

Radiative effects of CH₄, N₂O, halocarbons and the foreign-broadened H₂O continuum: A GCM experiment

M. Daniel Schwarzkopf and V. Ramaswamy

NOAA Geophysical Fluid Dynamics Laboratory, Princeton, New Jersey

Abstract. The simplified exchange approximation (SEA) method for calculation of infrared radiative transfer, used for general circulation model (GCM) climate simulations at the Geophysical Fluid Dynamics Laboratory (GFDL) and other institutions, has been updated to permit inclusion of the effects of methane (CH₄), nitrous oxide (N₂O), halocarbons, and water-vapor–air molecular broadening (foreign broadening). The effects of CH₄ and N₂O are incorporated by interpolation of line-by-line (LBL) transmissivity calculations evaluated at standard species concentrations; halocarbon effects are calculated from transmissivities computed using recently measured frequency-dependent absorption coefficients. The effects of foreign broadening are included by adoption of the “CKD” formalism for the water vapor continuum [Clough *et al.*, 1989]. For a standard midlatitude summer profile, the change in the net infrared flux at the model tropopause due to the inclusion of present-day concentrations of CH₄ and N₂O is evaluated to within ~5% of corresponding LBL results; the change in net flux at the tropopause upon inclusion of 1 ppbv of CFC-11, CFC-12, CFC-113, and HCFC-22 is within ~10% of the LBL results. Tropospheric heating rate changes resulting from the introduction of trace species (CH₄, N₂O, and halocarbons) are calculated to within ~0.03 K/d of the LBL results. Introduction of the CKD water vapor continuum causes LBL-computed heating rates to decrease by up to ~0.4 K/d in the upper troposphere and to increase by up to ~0.25 K/d in the midtroposphere; the SEA method gives changes within ~0.05 K/d of the LBL values. The revised SEA formulation has been incorporated into the GFDL “SKYHI” GCM. Two simulations (using fixed sea surface temperatures and prescribed clouds) have been performed to determine the changes to the model climate from that of a control calculation upon inclusion of (1) the trace species and (2) the foreign-broadened water vapor continuum. When the trace species are added, statistically significant warming (~1 K) occurs in the annual-mean tropical upper troposphere, while cooling (~1.5 K) is noted in the upper stratosphere and stratopause region. The changes are generally similar to annual-mean equilibrium calculations made using a radiative-convective model assuming fixed dynamical heating. The effects of the CKD water vapor continuum include cooling (~1 K) in the annual-mean troposphere above ~6 km, with significant warming in the lower troposphere. When effects of both trace gases and the CKD continuum are included, the annual-mean temperature increases below ~5 km and cools between 5 and 10 km, indicating that continuum effects dominate in determining temperature changes in the lower and middle troposphere. Above, trace gas effects dominate, resulting in warming in the tropical upper troposphere and cooling in most of the middle atmosphere. Clear-sky outgoing longwave irradiances have been computed for observed European Centre for Medium-Range Weather Forecasting atmospheric profiles using three versions of the SEA formulation, including the effects of (1) water vapor, carbon dioxide, and ozone; (2) the above species plus present-day concentrations of the new trace species; (3) all of the above species plus the CKD H₂O continuum. Results for all three cases are within ~10 W/m² of corresponding Earth Radiation Budget Experiment clear-sky irradiance measurements. The combined effect of trace gases and the CKD continuum result in a decrease of ~8 W/m² in the computed irradiances.

1. Introduction

Until recently, general circulation models (GCMs), used to model atmospheric climate, have employed methods for computing infrared radiative transfer which include the effects of carbon dioxide (CO₂), water (H₂O), and ozone (O₃), together

with clouds. It is well known [Intergovernmental Panel on Climate Change (IPCC), 1990; Ramanathan *et al.*, 1985] that the significant infrared opacity due to methane (CH₄) and nitrous oxide (N₂O), primarily in the 1200–1400 cm⁻¹ frequency band, contributes significantly to the longwave radiative balance of the Earth’s surface-troposphere system. In several previous modeling efforts the effects have either been neglected or simulated through the use of an effective amount of CO₂. The CO₂ amount has generally been taken to produce, on a global average, the same change in infrared irradiances at the top of

This paper is not subject to U.S. copyright. Published in 1999 by the American Geophysical Union.

Paper number 1999JD900003.

the atmosphere as would be obtained in stand-alone calculations explicitly including the effects of CH_4 and N_2O . The problem with this approach is that the altitude dependence of radiative heating changes due to CH_4 and N_2O is substantially different from that caused by CO_2 change [Clough *et al.*, 1995]. GCM simulations [Wang *et al.*, 1991] have also found substantial differences in the tropospheric response to radiative perturbations using these gases explicitly as compared to the response using effective amounts of CO_2 . Since the absolute concentrations of these species and their rates of increase differ substantially from that of the CO_2 concentrations, the accuracy of the depiction of climate evolution by climate models is enhanced by inclusion of the radiative effects of these gases.

Over the last 30 years, the atmospheric concentration of halocarbons, especially chlorofluorocarbons (CFCs), of anthropogenic origin, has substantially increased. In addition to the effects that these trace species have on the ozone concentration, various studies [Ramanathan *et al.*, 1985; Ramaswamy *et al.*, 1992; Christidis *et al.*, 1997] indicate a considerable radiative forcing and climate response to the introduction of present-day values of the CFCs, particularly CFC-11 and CFC-12. This occurs because these species have narrow but strong absorption bands in the 8–12 μm window region. It thus is important to include these radiative effects in GCM climate simulations, in addition to the effects of CO_2 , H_2O , O_3 , CH_4 , and N_2O .

One of the major difficulties in constructing an infrared radiative transfer algorithm in GCMs is the need to account for the effects of the “ H_2O continuum.” The need to include this continuum is a consequence of laboratory measurements of spectral H_2O opacity, together with opacity measurements performed in several field experiments. When these observations are compared to calculations which exclude contributions to H_2O opacities from “far wings” of the spectral line profile, the measurements show an excess opacity. For instance, line-by-line (LBL) flux computations, where the H_2O spectral line shape is taken as Lorentzian but “cut off” at 3 cm^{-1} from the line center, underestimate the downward infrared surface flux by $\sim 40 \text{ W/m}^2$ for a clear-sky midlatitude summer case [Ellingson *et al.*, 1991]. The deficiency is most evident in frequency ranges, such as the 8–12 μm window region, where local H_2O spectral line strengths are weak. This opacity has been attributed either to the presence of H_2O - H_2O dimers [Suck *et al.*, 1979] or to enhanced absorption from far wings of H_2O lines due to molecular broadening [Clough *et al.*, 1980]. The molecular broadening may result from either foreign broadening (water-vapor-air collisions) or self-broadening (water vapor-water vapor collisions).

The current generation of infrared radiative transfer algorithms in most climate GCMs generally relies on a method devised by Roberts and coworkers [Roberts *et al.*, 1976 (hereinafter referred to as the RSB algorithm)]. This approach assumes that the H_2O continuum is caused by self-broadening, ascribed to the existence of H_2O - H_2O dimers. An extensive set of laboratory data [Burch, 1981; Burch and Alt, 1984] has indicated that self-broadening is indeed the dominant cause of the H_2O continuum in the 8–12 μm window region. However, in other spectral regions, there remains an unexplained excess opacity. In an important development, Clough *et al.* [1989] demonstrated the importance of including a foreign-broadened H_2O continuum in these regions and developed a formalism enabling the calculation of the effects of water vapor

lines and of the self-broadened and foreign-broadened water vapor continuum in a consistent manner. In this formulation, a method is developed to divide the H_2O spectral line shape into two parts, one of which represents the contributions from H_2O lines and the remainder, which constitutes the “CKD” continuum. LBL calculations [Clough *et al.*, 1992] indicate that the use of the CKD continuum significantly decreases upper tropospheric heating rates. Since this may alter upper tropospheric temperatures and moisture amounts in climate simulations, the inclusion of a formulation for the CKD continuum in GCMs becomes a matter of substantial interest.

At GFDL the principal tool for studying the troposphere-stratosphere-mesosphere system has been the SKYHI general circulation model. A detailed description of this model and its climatology is found in the work of Hamilton *et al.* [1995]. The shortwave radiative transfer algorithm in the SKYHI GCM follows Lacis and Hansen [1974] as modified by Ramaswamy and Freidenreich [1992] to account accurately for water vapor absorption at small path lengths. The infrared radiative algorithm of the GCM has been described by Schwarzkopf and Fels [1991] (hereinafter referred to as SF91). The basic method is the “simplified exchange” approximation (SEA) [Fels and Schwarzkopf, 1975 (hereinafter referred to as SF75), 1981; Schwarzkopf and Fels, 1985 (hereinafter referred to as SF85)]. In this algorithm the only radiatively active gases are H_2O , CO_2 , and O_3 ; the H_2O continuum is treated using the RSB method. The standard CO_2 concentration used in all SKYHI calculations to date is 330 ppmv. The exclusive use of this concentration, rather than an “effective CO_2 ” concentration, confirms that results from SKYHI calculations have not included in any manner thus far the radiative effects of CH_4 , N_2O , and halocarbons and of the foreign-broadened H_2O continuum.

From the preceding discussion it is apparent that the inclusion of the effects of CH_4 , N_2O , and halocarbons, as well as a more accurate depiction of the effects of continuum absorption by water vapor, is highly desirable. This paper is primarily concerned with the development of a revised SEA formulation which includes these effects, yet remains sufficiently accurate and rapid to allow inclusion in climate GCMs. Section 2 describes the changes made to obtain the new version of the SEA formulation. Separate descriptions are given for the algorithms for CH_4 and N_2O , halocarbons, and the CKD water vapor continuum. In each case, heating rate and flux computations are validated by comparison with line-by-line calculations. In section 3, the results of GCM calculations, including the effects of CH_4 , N_2O , and halocarbons, are compared to GCM results lacking these radiative effects. Section 4 discusses GCM calculations showing the effects of inclusion of the new algorithm for the water vapor continuum. In section 5, clear-sky outgoing longwave irradiances using the SEA formulation are compared with satellite irradiance observations for the same locations. A summary of the GCM results and conclusions comprise section 6.

2. Radiative Transfer Algorithm

2.1. Overview of the SEA Method

The SEA method (first introduced in SF75) is based on the premise that infrared heating rates due to water vapor absorption may be computed by (1) separating the heating rate into a cooling-to-space (CTS) term, including the effects of photon escape from an atmospheric layer to space and an exchange term, incorporating photon exchange with other atmospheric

layers; (2) assuming that the heating rate due to the exchange term may be approximated by a broadband emissivity calculation, dependent only on a scaled mass and temperature between atmospheric levels. This assumption leads to the following relation:

$$Q = Q^{\text{APPROX}} - Q_{\text{CTS}}^{\text{APPROX}} + Q_{\text{CTS}}, \quad (1)$$

where Q is the heating rate, Q^{APPROX} is the heating rate from the broadband calculation, $Q_{\text{CTS}}^{\text{APPROX}}$ is the CTS term calculated using the broadband calculation, and Q_{CTS} is the CTS term computed using an "exact" parameterization, in practice a narrowband Goody random model [Rodgers and Walshaw, 1966]. Extension of the method to include other species and to include the water vapor continuum is accomplished by modifying the definitions of the heating rate terms in (1). In frequency domains, where water vapor is the only significant absorber, the definitions given above apply. In other frequency domains, each heating rate term in (1) is computed using appropriate transmission functions, which in turn are products of transmissivities of each of the absorbing species included in that frequency domain. In practice, H_2O absorption in the microwave region ($0\text{--}160\text{ cm}^{-1}$) and in the vibration-rotation band ($1200\text{--}2200\text{ cm}^{-1}$) are treated by assuming that $Q \approx Q^{\text{APPROX}}$. This leads to the following relations:

$$Q = Q^{\text{APPROX}} \quad (0\text{--}160, 1200\text{--}2200\text{ cm}^{-1}) \quad (2a)$$

$$Q = Q^{\text{APPROX}} - Q_{\text{CTS}}^{\text{APPROX}} + Q_{\text{CTS}} \quad (160\text{--}560\text{ cm}^{-1}) \quad (2b)$$

$$Q = Q^{\text{GASES}} - Q_{\text{CTS}}^{\text{GASES}} + Q_{\text{CTS}} \quad (560\text{--}1200\text{ cm}^{-1}). \quad (2c)$$

Here Q^{GASES} and $Q_{\text{CTS}}^{\text{GASES}}$ are heating rate terms over broad frequency bands, which include the effects of all primary absorbers in the band.

The principal advantage of the SEA method is that the Q_{CTS} term, which depends only on transmissivities between a pressure level and space, may be computed on rather narrow frequency bands with a relatively small expenditure of computation time. In evaluating this term, effects not accounted for in the Q^{APPROX} , $Q_{\text{CTS}}^{\text{APPROX}}$, Q^{GASES} , and $Q_{\text{CTS}}^{\text{GASES}}$ terms in (2a)–(2c), such as the dependence of water vapor line intensity and line width on temperature, may be included. The second advantage is that the effects of many secondary absorbers may be captured by inclusion of their narrowband transmission functions in the Q_{CTS} term, at little cost and with sufficient accuracy. Thus in the version of the SEA formulation described in SF91, the Q_{CTS} term is used to include the effects of H_2O continuum absorption in the $400\text{--}800\text{ cm}^{-1}$ range and the contributions of H_2O lines in the $8\text{--}12\text{ }\mu\text{m}$ window region. In SF91, clear-sky heating rates, including the effects of H_2O , CO_2 , and O_3 and with the H_2O continuum effects computed using the RSB algorithm, were obtained using (2a)–(2c) and compared to corresponding LBL calculations on standard profiles; the close agreement confirmed the accuracy of the method. So long as clouds are assumed to be gray absorbers, their effects are easily incorporated by simple multiplication of the gaseous and cloud transmission functions used in obtaining each term of (2a)–(2c).

The disadvantage of the SEA method stems from the requirement that in the frequency ranges where water vapor is not the dominant gaseous absorber, separate heating rate calculations must be undertaken using (2c), each of which may be as time consuming as that for the water vapor band (equations (2a)–(2b)). In each such frequency range, a transmission func-

tion must be obtained for each absorbing species. For H_2O and ozone, both of which have concentrations varying in altitude and time, approximate narrowband models are used to obtain the desired band transmissivities. For a species such as CO_2 which has an essentially height-invariant concentration which changes slowly in time, one may use transmissivities precomputed using LBL methods, at the appropriate concentration and vertical resolution. The band transmission function then is the product of the species transmissivities (and the cloud transmissivity). The resultant transmission function may be used to compute the terms in (2c); in some frequency ranges, the effects of secondary absorbers may be included only in transmissivities employed in computing the Q_{CTS} term. The frequency ranges and the primary and secondary absorbers included in the SEA formulation described in SF91 are given in Tables 1 and 3 of that paper.

2.2. Inclusion of CH_4 and N_2O

Inclusion of CH_4 and N_2O in the SEA formulation requires several modifications to the methods outlined above. In the infrared spectrum, the most important band system of N_2O is the $7.8\text{ }\mu\text{m}$ system (centered at $\sim 1285\text{ cm}^{-1}$). The $17\text{ }\mu\text{m}$ band system (centered at $\sim 589\text{ cm}^{-1}$) also possesses substantial band intensity. The strongest CH_4 band system is centered at $\sim 1311\text{ cm}^{-1}$. Spectral lines of these two molecules of sufficient strength to produce significant terrestrial atmospheric opacity are present throughout the $1200\text{--}1350\text{ cm}^{-1}$ frequency range, with N_2O lines also extending to $\sim 1125\text{ cm}^{-1}$ and CH_4 lines to $\sim 1400\text{ cm}^{-1}$ [Goody and Yung, 1989, chapter 5]. In consequence, the $1200\text{--}1400\text{ cm}^{-1}$ range, which (in SF91) is subsumed into the only frequency range where water vapor absorption dominates, must be treated separately from the remainder of the H_2O vibration-rotation band. In addition, the presence of the $17\text{ }\mu\text{m}$ N_2O band system within the frequency range ($560\text{--}800\text{ cm}^{-1}$) of the CO_2 $15\text{ }\mu\text{m}$ band complex suggests a need to modify the band structure used in that range.

After considerable experimentation, it was determined that the effects of CH_4 and N_2O in the $1200\text{--}1400\text{ cm}^{-1}$ frequency range may be simulated, to sufficient accuracy, by employing LBL transmission functions of CH_4 and of N_2O computed over one frequency band ($1200\text{--}1400\text{ cm}^{-1}$) comprising that frequency range. As in the case of CO_2 (discussed in SF85), the LBL transmissivities are obtained for several standard concentrations of CH_4 and N_2O using a high vertical resolution (at present 496 vertical levels). The transmissivities (for a standard temperature profile) are interpolated to the desired vertical level structure (which may vary in space and time) and concentration using a revised version of the algorithm developed in SF85. A discussion of the modifications and of their application to CH_4 and N_2O will be presented in a forthcoming paper.

The effects of H_2O absorption in the $1200\text{--}1400\text{ cm}^{-1}$ range are evaluated using broadband emissivity calculations to obtain H_2O transmissivities, as in SF75 (their equations (4)–(5)) but including only the $1200\text{--}1400\text{ cm}^{-1}$ range. A separate broadband emissivity calculation is required to obtain H_2O transmissivities for the remainder of the water-vapor-dominated frequency range. The overall transmission function in the $1200\text{--}1400\text{ cm}^{-1}$ range, including the effects of H_2O , CH_4 , and N_2O is obtained as the product of the species transmissivities.

The N_2O $17\text{ }\mu\text{m}$ system is located in a frequency range in which most of the opacity is due to strong spectral lines of CO_2 and H_2O . The effects of the N_2O system will thus be noticeable mostly in the middle atmosphere, where line overlap is reduced

Table 1. Comparison of Line-by-Line and Parameterized Net Fluxes: Effects of CH₄ and N₂O

Method and Altitude	CH ₄ , N ₂ O: 1200–1400 cm ⁻¹	N ₂ O: 1070–1200 cm ⁻¹	N ₂ O: 560–630 cm ⁻¹
LBL, top	-3.50	-0.29	-0.39
LBL, tropopause	-3.44	-0.23	-0.48
LBL, surface	-1.49	-0.19	-0.01
SEA, top	-3.38	-0.26	-0.40
SEA, tropopause	-3.31	-0.28	-0.53
SEA, surface	-1.88	-0.34	-0.00

Comparison of changes in net flux (W/m²) computed by the line-by-line (LBL) and simplified exchange approximation (SEA) methods upon introduction of 1.75 ppmv of CH₄ and 0.28 ppmv of N₂O. The reference flux calculations include only effects due to H₂O, CO₂, and O₃.

and H₂O concentrations are smaller. It thus is reasonable to include its effects only as part of the Q_{CTS} term for the frequency domain of interest. In SF91 the 15 μm band frequency range (560–800 cm⁻¹) was divided into two bands (560–670 and 670–800 cm⁻¹; see their Table 3). To include the N₂O 17 μm system, the 560–800 cm⁻¹ range has now been split into three bands: (1) 560–630 cm⁻¹, which includes the N₂O 17 μm system; (2) 630–700 cm⁻¹; (3) 700–800 cm⁻¹. This division has the further advantage of separating the CO₂ fundamental band (with little temperature dependence) from the hot bands (with strong temperature dependence). The effects of this division on the calculation of CO₂ transmissivities will be discussed in a forthcoming paper.

In the 1070–1200 cm⁻¹ frequency range, where the opacity is mostly due to the effects of the H₂O continuum, the effects of the N₂O lines have been accounted for by including the species transmissivity in the Q_{CTS} term computed for this range.

The considerations discussed above lead to the following relations to describe the new SEA formulation:

$$Q = Q^{\text{APPROX}}(I) \quad (0-160, 1400-2200 \text{ cm}^{-1}) \quad (3a)$$

$$Q = Q^{\text{APPROX}}(I) - Q_{\text{CTS}}^{\text{APPROX}} + Q_{\text{CTS}} \quad (160-560 \text{ cm}^{-1}) \quad (3b)$$

$$Q = Q^{\text{GASES}} - Q_{\text{CTS}}^{\text{GASES}} + Q_{\text{CTS}} \quad (560-1200 \text{ cm}^{-1}) \quad (3c)$$

$$Q = Q^{\text{APPROX}}(II) \quad (1200-1400 \text{ cm}^{-1}). \quad (3d)$$

In (3a)–(3b), $Q^{\text{APPROX}}(I)$ refers to the heating rate obtained using H₂O broadband emissivities appropriate to the frequency range; $Q^{\text{APPROX}}(II)$ refers to the heating rate for the 1200–1400 cm⁻¹ range obtained by combining the effects of H₂O, CH₄, and N₂O. In the remainder of this paper, the SEA formulation will refer to heating rates obtained using (3a)–(3d).

To test the validity and accuracy of the new SEA formulation, LBL computations (using 122 vertical layers) have been compared to SEA calculations (with 40 vertical layers) for a standard midlatitude summer (MLS) profile. Table 1 displays the computed changes in the net flux (in W/m²) at the top of the atmosphere, tropopause, and surface due to the introduction of 1.75 ppmv of CH₄ and 0.28 ppmv of N₂O (approximately the current concentrations) using the LBL approach and the new SEA formulation. The reference calculations include only the effects of H₂O (with a “cutoff” Lorentzian spectral line shape and a continuum treated using the RSB formulation), CO₂, and O₃. The LBL results for the entire infrared spectrum agree with expectations [IPCC, 1990] for the instantaneous radiative forcing to within ~5%.

In the 1200–1400 cm⁻¹ range (Table 1, column 2) the SEA

algorithm reproduces the LBL flux results to within ~5% at the top and the tropopause and to ~25% at the surface. To investigate the cause of the larger percentage errors at the surface upon introduction of CH₄ and N₂O, a series of calculations using the SEA method as well as a random model formulation were performed in which the number of bands in this frequency range (of equal bandwidths) was increased from unity. The absolute value of changes in surface fluxes was found to decrease by ~0.8 W/m² (~40%) as the number of bands increased from 1 to 4. The results using four bands agree most closely with the LBL values. It is thus likely that the effects of overlap between the CH₄ and the N₂O lines (which decrease in intensity with increasing wavenumber) and the H₂O lines (which increase in intensity with increasing wavenumber) are the major factors in explaining the differences between the LBL and the SEA results for the surface flux changes. By contrast, these calculations indicate that the change in net flux at the tropopause due to introduction of CH₄ and N₂O varies by only ~15% when the band numbers are increased and that the results using one band are as close to the LBL values as those for four bands. Parallel calculations using tropical and subarctic winter atmospheric profiles (with one band) establish that percentage errors in flux changes at the top and the tropopause remain below ~5%; the percentage error at the surface is small for the subarctic winter case but increases to ~50% (~0.5 W/m²) for the tropical case. Since the tropopause flux change is the most significant quantity in estimating the radiative forcing of the Earth-atmosphere system [IPCC, 1994], it is justifiable to use the one-band formulation which requires the least amount of computer time.

Table 1 (column 3) displays the flux changes computed with the LBL and the parameterized methods due to the inclusion of N₂O in the 1070–1200 cm⁻¹ frequency range. The only significant error is in the surface flux. The principal reason is that the CTS approximation used to evaluate the effects of inclusion of N₂O on the fluxes neglects photon exchanges between the atmospheric layers and the surface, which is very significant when spectral line absorption is weak, as in this frequency region. Again, however, an accurate calculation of flux changes at the tropopause is more significant in estimating the climatic effects of N₂O than the surface error (which in any case is only ~0.15 W/m²). The effects of inclusion of the N₂O 17 μm system are shown in Table 1 (column 4); the LBL and SEA formulations give flux changes agreeing to within ~10% at all altitudes.

Figure 1 displays the heating rate changes over the entire infrared spectrum (0–2200 cm⁻¹) resulting from the introduction of CH₄ and N₂O using the LBL and SEA methods for an

Figure 1. (opposite) Comparison of line-by-line (LBL) (solid line) and simplified exchange approximation (SEA) (solid line with filled circles) heating rate calculations (in Kelvins per day (K/d)) for the standard midlatitude summer (MLS) profiles, with three cloud layers included. (a, b) Heating rates obtained when only the radiative effects of CO₂, H₂O, and ozone are included, and H₂O continuum effects are evaluated using the RSB method (three-gas (3gas)); Figures 1a emphasizes the middle atmosphere and (1b) the troposphere. (c, d) Differences in LBL and SEA heating rates from results in Figures 1a and 1b, respectively, upon inclusion of CH₄ and N₂O effects. (e, f) Similar to Figures 1c and 1d but with the additional inclusion of the effects of CFC-11, CFC-12, CFC-113, and HCFC-22 (9gas).

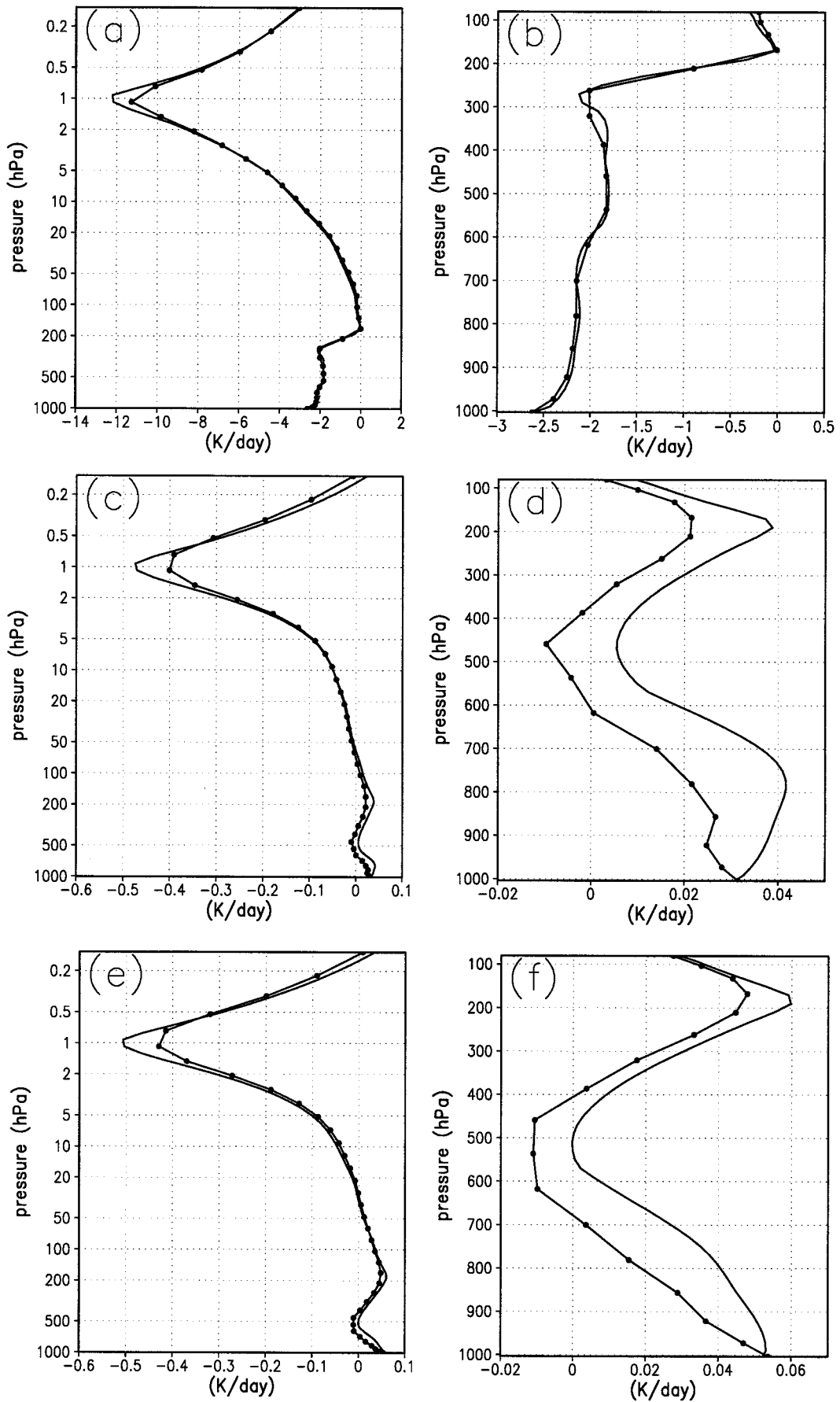


Table 2. Comparison of Line-by-Line and Parameterized Net Fluxes: Effects of Halocarbons

Method and Altitude	CFC-11, CFC-12		CFC-11, CFC-12, CFC-113, HCFC-22	
	560–1200 cm ⁻¹	0–2200 cm ⁻¹	560–1200 cm ⁻¹	0–2200 cm ⁻¹
LBL, top	-0.97	-0.97	-1.77	-1.81
LBL, tropopause	-0.77	-0.77	-1.42	-1.44
LBL, surface	-0.65	-0.65	-1.18	-1.19
SEA, top	-1.07		-2.03	
SEA, tropopause	-0.80		-1.53	
SEA, surface	-0.65		-1.23	

Comparison of changes in net flux (in W/m²) computed by the LBL and SEA methods upon introduction of 1 ppbv of CFC-11, CFC-12, CFC-113, and HCFC-22. The reference flux calculations include only effects due to H₂O, CO₂, and O₃.

MLS profile. For reference, Figures 1a and 1b show the heating rates when the only absorbers are H₂O lines, the H₂O continuum (evaluated using the RSB algorithm), CO₂, and O₃. Inspection of Figure 1c indicates that the SEA method reproduces the LBL heating rate changes to within ~10% in the middle atmosphere, with errors generally being less than 0.02 K/d. In the troposphere (Figure 1d) the fractional errors are larger, with the SEA method giving heating rate changes ~0.01–0.02 K/d less than the changes computed using the LBL method. In both methods, heating rate changes are largest near the surface and in the upper troposphere. As with the flux results, the differences in heating rates between the SEA and the LBL values are probably due to the use of a one-frequency band in the 1200–1400 cm⁻¹ frequency range.

2.3. Inclusion of Halocarbons

Infrared radiative effects of the chlorofluorocarbons (CFCs) and hydrochlorofluorocarbons (HCFCs) are the result of absorption bands, principally in the 600–1400 cm⁻¹ frequency range. LBL calculations, begun as part of the ICRCCM (Intercomparison of Radiation Codes in Climate Models) study [Ellingson *et al.*, 1991], have been extended to include the effects of CFCs and HCFCs over the entire infrared frequency range (0–2200 cm⁻¹). These calculations use CFC and HCFC absorption coefficients, with a spectral resolution of 0.1 cm⁻¹, obtained by Magid [Fisher *et al.*, 1990]. For the clear-sky MLS profile, the flux change at the tropopause (instantaneous clear-sky radiative forcing) is 0.35 W/m² upon introduction in the entire atmospheric column of 1 ppbv of CFC-11. This value agrees with recent calculations for a global, annual-mean profile [Christidis *et al.*, 1997] and is larger than the IPCC estimate [IPCC, 1994]. LBL results for tropopause flux changes upon introduction in the entire atmospheric column of 1 ppbv of CFC-11 and CFC-12 and for introduction of 1 ppbv of CFC-11, CFC-12, CFC-113, and HCFC-22 are shown in Table 2; in both situations the computed changes are within ~10% of the values expected if the radiative forcing per unit molecule relative to CFC-11 is taken from the IPCC [1994] values and the Magid value for the instantaneous clear-sky radiative forcing is adopted (the changes are reduced if the halocarbon concentrations are lowered in the middle atmosphere [Christidis *et al.*, 1997]). Again, the reference calculations include only the effects of H₂O, CO₂, and O₃.

If present-day concentrations of the halocarbon species are employed [IPCC, 1994] together with the IPCC values of rel-

ative radiative forcing per unit molecule, the four halocarbon species considered above are responsible for ~90% of the flux change at the tropopause attributable to the introduction of all CFCs and HCFCs. As a result, the new SEA formulation has been designed to include the effects of only these four halocarbons. The algorithm assumes that the absorption increases linearly with the amount; that is, the species is in the “weak line” limit. Ramanathan *et al.* [1985] have demonstrated that this is a reasonable assumption. Angular integration of the halocarbon transmissivities is performed using a diffusivity factor of 2, in agreement with theory for this limit. A further approximation is to confine the effects of the halocarbons to the 560–1200 cm⁻¹ frequency range. The effects of all four halocarbons are included in the first two (broadband) terms in (3b)–(3c); the effects of a particular halocarbon is included in the Q_{CTS} term in (3b)–(3c) if the species has a nonzero absorption coefficient in a frequency band within the 560–1200 cm⁻¹ range.

The bottom part of Table 2 gives the flux changes at the top of the atmosphere, tropopause, and surface computed with the SEA formulation upon introduction of CFC-11 and CFC-12 only and upon introduction of all four halocarbons. The concentrations of all CFC and HCFC species are 1 ppbv. Comparison of the LBL and SEA results for CFC-11 and CFC-12 and for all four halocarbons shows that the flux changes agree to within ~10% at all altitudes. This indicates that the use of the weak-line approximation for halocarbon transmissivities in the SEA formulation is an acceptable assumption. Differences between the LBL and the SEA calculations for flux changes at the tropopause would be greatly reduced if current halocarbon concentrations [IPCC, 1995] were used, since the effect of each halocarbon scales almost linearly with concentration.

Figures 1e–1f display the changes in heating rates computed using the LBL and the new SEA formulation when CH₄, N₂O, and the four halocarbons have been included (at concentrations of 1 ppbv). In the troposphere the heating rate changes have been reproduced to within ~0.02 K/d. Comparison of Figures 1d and 1f indicates that in the troposphere the errors in the SEA formulation with CH₄, N₂O, and halocarbon species included are slightly smaller in magnitude to those including only CH₄ and N₂O. In the middle atmosphere, addition of the four halocarbons has little effect on errors in the computed heating rates (see Figures 1c and 1e).

2.4. Inclusion of the CKD Water Vapor Continuum

The version of the CKD water vapor continuum model [Clough *et al.*, 1989, 1992] adopted for the SEA formulation is the “CKD2.1” version (denoted henceforth as the CKD model). The procedure for replacement of the previous (RSB) continuum algorithm [Roberts *et al.*, 1976] by the CKD model entails formulation of an algorithm which gives flux and heating rate changes agreeing with those obtained using line-by-line methods. To do this, LBL flux and heating rate calculations for the MLS clear-sky atmospheric profile, where the water vapor continuum absorption is computed using the CKD formulation, have been compared to LBL calculations on the identical atmospheric profile but using the RSB algorithm. Figure 2 displays the differences between the CKD and the RSB calculations for the accumulated heating rate $Q(\nu) = \sum_1^N Q_n$, where Q_n is the heating rate over a 10 cm⁻¹ wide wavenumber band, and the sum is taken over N wavenumber bands, including all wavenumbers from 0 to ν . Results are displayed for wavenumbers below 1200 cm⁻¹. From ~200 cm⁻¹ the

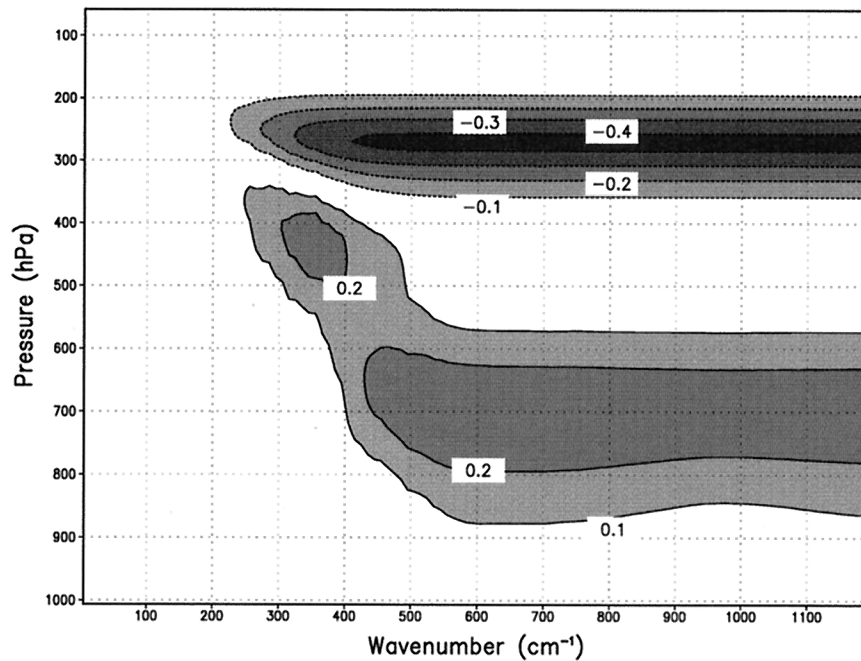


Figure 2. Difference in the accumulated heating rates (in K/d), summed from 0 cm^{-1} to a specified wavenumber between LBL calculations for the MLS profile using the CKD and RSB methods to evaluate the H_2O continuum effects. For frequencies greater than $\sim 500 \text{ cm}^{-1}$ the CKD calculations show more cooling near $\sim 250 \text{ hPa}$ and less cooling near $\sim 700 \text{ hPa}$.

inclusion of a foreign-broadened continuum in the CKD algorithm results in increased cooling in the upper troposphere (200–300 hPa) and heating below. The continuum has its greatest influence on heating rates at altitudes where absorption due to H_2O lines becomes relatively weak. Above this point, the continuum contributes to cooling to space, resulting in decreased heating rates; below, increased downward fluxes cause a heating, which is important until opacities from water vapor lines become the dominant contribution to the heating rates. As water vapor line strengths tend to decrease with increasing wavenumber, the altitude of the transition from cooling to heating due to the continuum decreases, and the altitude range where continuum heating is noticeable grows larger. By $\sim 560 \text{ cm}^{-1}$ the region of greatest heating is in the middle troposphere (600–750 hPa). At wavenumbers greater than $\sim 560 \text{ cm}^{-1}$ the self-broadened water vapor continuum becomes dominant; its effects have already been accounted for in the RSB formulation. Thus only minor changes in $Q(\nu)$ are seen at these wavenumbers. The heating rate changes shown here are quite similar to the differences obtained by Clough *et al.* [1992, Figure 19] for the entire infrared spectrum; surface, tropopause, and top of the atmosphere fluxes agree with values reported by Clough *et al.* [1992] to within $\sim 2 \text{ W/m}^2$ at all levels.

At wavenumbers beyond 1200 cm^{-1} the effects of foreign broadening again become dominant in the CKD continuum formulation. For purposes such as retrieval of irradiances the inclusion of the continuum in these frequencies may be important, especially in narrow window regions (e.g., near $\sim 1590 \text{ cm}^{-1}$). However, the smaller value of the Planck function at these wavenumbers, together with the presence of nearby strong spectral water vapor lines, makes the inclusion of a continuum absorption in these frequencies relatively unimportant in climate GCMs. This is illustrated in Figure 3a, which gives the difference in heating rates between LBL calculations

using the CKD and the RSB methods calculations for the MLS clear-sky atmospheric profile over the entire infrared spectrum (here $0\text{--}3000 \text{ cm}^{-1}$). The CKD calculations produce an increased cooling in the upper troposphere (up to $\sim 0.45 \text{ K/d}$ at 270 hPa) and warming in the middle troposphere (reaching $\sim 0.28 \text{ K/d}$ at 700 hPa). These results are essentially the same as the values of $Q(\nu = 1200 \text{ cm}^{-1})$ displayed in Figure 2, indicating that the continuum has little effect on heating rates beyond this frequency. The change in the net (up-down) LBL clear-sky infrared flux computed using the CKD and the RSB algorithms over the $0\text{--}3000 \text{ cm}^{-1}$ range is shown in Figure 3b as a function of altitude; at the top of the atmosphere the use of the CKD algorithm results in a decrease of $\sim 4.5 \text{ W/m}^2$.

The SEA H_2O continuum formulation is based on the formalism of the CKD method but has been limited to the $160\text{--}1200 \text{ cm}^{-1}$ frequency range in accordance with the LBL results. Following Clough *et al.* [1989] the continuum absorption coefficient $k_c(\nu, T)$ may be written as

$$k_c(\nu, T) = R(\nu, T) \cdot \left[k_{\text{self}}(\nu, T) \left(\frac{\rho_s}{\rho_0} \right) + k_f \left(\frac{\rho_f}{\rho_0} \right) \right]. \quad (4)$$

Here $R(\nu, T)$ is the “radiation function,” including effects of stimulated emission, defined as

$$R(\nu, T) = \nu \tanh(\beta\nu/2). \quad (5)$$

In (4) and (5), ν is the wavenumber and T is the temperature; $\beta = hc/kT$, k_{self} and k_f are the self-broadened and foreign-broadened spectral density functions, respectively; ρ_s and ρ_f are the H_2O and air densities, respectively; and ρ_0 is the standard atmospheric density. The constants h , c , k are the Planck constant, the velocity of light, and the Boltzmann constant, respectively. The temperature dependence of k_{self} may be written as

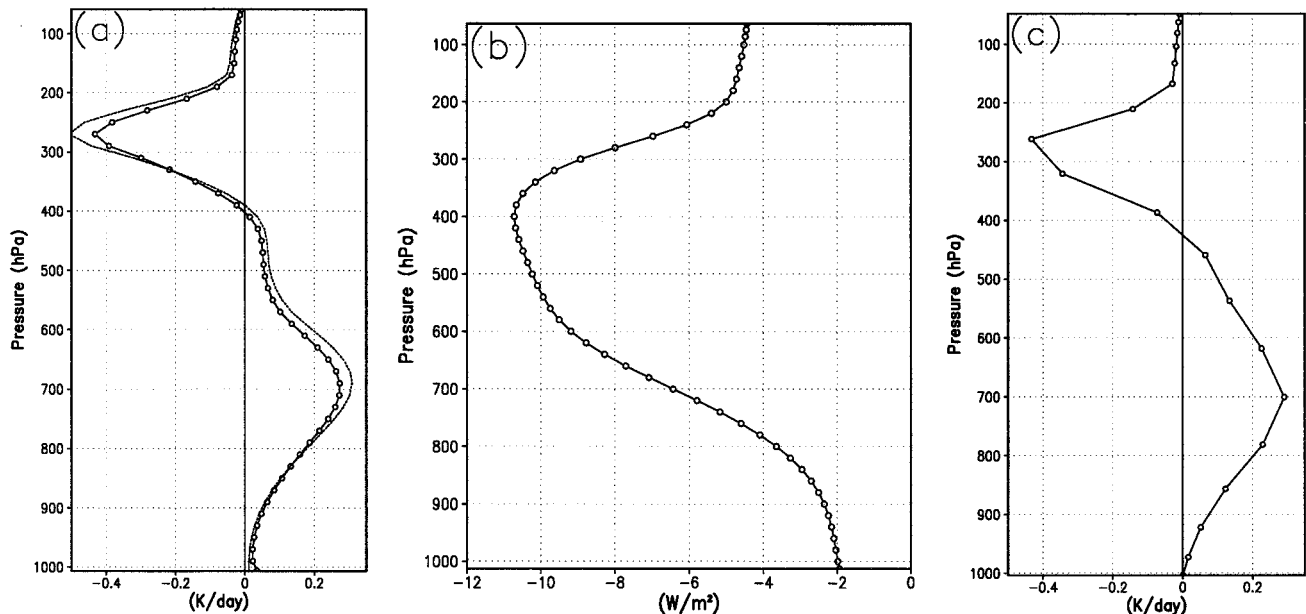


Figure 3. Difference between infrared heating rates (in K/d) and net fluxes (in Watts per square meter (W/m^2)) using the CKD and RSB methods to evaluate H_2O continuum effects for an MLS profile. (a, c) Heating rate differences using the (a) LBL or (c) SEA methods; Figure 3b gives changes in net fluxes using the LBL method. The dotted line in Figure 3a is the LBL result when heating rates are computed using the CTS approximation.

$$k_{\text{self}}(\nu, T) = k_{\text{self}}(\nu, 296) \cdot \exp[-c(\nu)(T - 296)] \quad (6)$$

with $k_{\text{self}}(\nu, 296)$ and $c(\nu)$ being experimentally determined quantities. The foreign-broadened spectral density function is assumed to have no temperature dependence.

In the present formulation, additional simplifications are applied to (5) and (6). In frequency bands in the $160\text{--}560\text{ cm}^{-1}$ range, the radiation function is computed using (5); however, in frequency bands at higher wavenumbers, $R(\nu, T)$ has been assumed to be temperature independent. This approximation is justifiable because $R(\nu, T)$ approaches unity with increasing wavenumber and exceeds ~ 0.90 at wavenumbers greater than $\sim 560\text{ cm}^{-1}$ for terrestrial temperatures. After considerable experimentation, $c(\nu)$ in (6) has been set to 0.013 for all wavenumber bands in the $160\text{--}560\text{ cm}^{-1}$ range and to 0.020 for bands between 560 and 1200 cm^{-1} . The temperature dependence adopted for the self-broadened continuum in the $8\text{--}12\ \mu\text{m}$ range is thus the same as that of the RSB formulation in the same range.

Inclusion of the CKD continuum absorption into the SEA formulation (equations (3a)–(3d)) is accomplished by including the effects in the Q_{CTS} term in the $160\text{--}560\text{ cm}^{-1}$ frequency range (equation (3b)) and in all terms in the $560\text{--}1200\text{ cm}^{-1}$ range (equation (3c)). This specification incorporates an important assumption: the effects of the CKD continuum on heating rates and fluxes in the $160\text{--}560\text{ cm}^{-1}$ range are largely due to cooling to space. The plausibility of this assumption is demonstrated using parallel LBL calculations (shown as a dotted line in Figure 3a) in which CKD and RSB heating rate calculations are obtained using only the Q_{CTS} term. The differences between the CKD and the RSB heating rates computed in this manner are within $\sim 0.05\text{ K/d}$ of the differences obtained when all heating rate terms are included. Use of this assumption results in a large saving in computation time, since

there is no need to change the methods for calculation of the first two terms of (3b).

In the $160\text{--}560\text{ cm}^{-1}$ range, the continuum absorption coefficient (defined in (4)) generally decreases with frequency; the variation is generally uncorrelated with the more rapid frequency variations of the H_2O line absorption coefficient. To minimize errors resulting from this effect, frequency bands used to compute the Q_{CTS} term in (3b) have each been made 10 cm^{-1} wide; the total number of bands in this frequency range is thus 40. This represents a substantial increase from the eight bands used in the previous formulation (SF91, Table 3). Although this change results in a small increase in computation time, the advantages of greater algorithm simplicity, increased accuracy in the computed heating rates, and improved capability to obtain top of the atmosphere irradiances in this frequency range justify the new approach.

In the $560\text{--}1200\text{ cm}^{-1}$ frequency range, the introduction of the CKD continuum does not require changes in the frequency band structure, beyond that already done for introduction of CH_4 and N_2O . The effects of the CKD continuum are included in all terms of (3c) in conjunction with the effects of other absorbing species.

Figure 3c displays the result of heating rate calculations on a clear-sky MLS profile using the SEA formulation using the CKD method, compared to SEA calculations using the RSB method. In each case, the effects of CH_4 , N_2O , and halocarbons were included. The results show that the CKD calculation produces a substantial additional cooling tendency in the upper troposphere, together with heating below. These differences between the CKD and the RSB calculations are quite similar to those from the corresponding LBL calculations (Figure 3a); the SEA and LBL differences generally agree to within $\sim 0.05\text{ K/d}$.

Table 3. New Formulation

Frequency Range, cm^{-1}	APPROX	CTS
0–160	1 band used for 0–560, 1400–2200 cm^{-1} range; H_2O lines using emissivity calculation	none
160–560	as in 0–160 cm^{-1} range	40 bands: H_2O lines, CKD continuum
560–800	1 band; H_2O lines, CKD continuum, LBL-derived CO_2 , $14 \mu\text{m}$ N_2O , 4 halocarbons	3 bands: $14 \mu\text{m}$ N_2O in 560–630 cm^{-1} band, H_2O lines, CKD continuum, CO_2 , 4 halocarbons
800–990	1 band for 800–990, 1070–1200 cm^{-1} range; CKD H_2O continuum, 4 halocarbons	2 bands: H_2O lines, CKD continuum, 4 halocarbons
990–1070	1 band; O_3 , CKD continuum, 4 halocarbons	1 band; O_3 , H_2O lines, CKD continuum, 4 halocarbons
1070–1200	as in 800–990 cm^{-1} range	1 band; H_2O lines, CKD continuum, N_2O , 4 halocarbons
1200–1400	1 band; H_2O lines using emissivity calculation, LBL-derived CH_4 , N_2O	none
1400–2200	as in 0–160 cm^{-1} range	none

Summary of features of the SEA formulation. Column 1 gives the main frequency ranges employed. Column 2 gives the primary absorbers and algorithms used for broadband calculations (such as Q^{APPROX}) in each main frequency range. Column 3 gives the primary absorbers and algorithms used for narrowband cooling to space (Q_{CTS}) calculations in each main frequency range.

2.5. Additional Changes and Summary

A number of changes have been made to the SEA formulation, not related to the modifications discussed in sections 2b–2d: (1) Spectral line data for H_2O , CO_2 , O_3 , CH_4 and N_2O are now based on the HITRAN 92 catalog [Rothman *et al.*, 1992]; (2) the techniques for incorporating cloud effects now permit the existence of both maximally overlapped and randomly overlapped clouds; (3) significant improvements have been made in code modularity and efficiency. The computer time required for heating rate calculations using the new algorithm has increased by only $\sim 50\%$, despite the necessity for two emissivity calculations for water vapor (see (3a) and (3d)) and the introduction of several transmissivity computations for added species. This burden should not be excessive for most numerical models, considering the substantial gain in accounting accurately for the radiative effects of several climatically significant absorbing species.

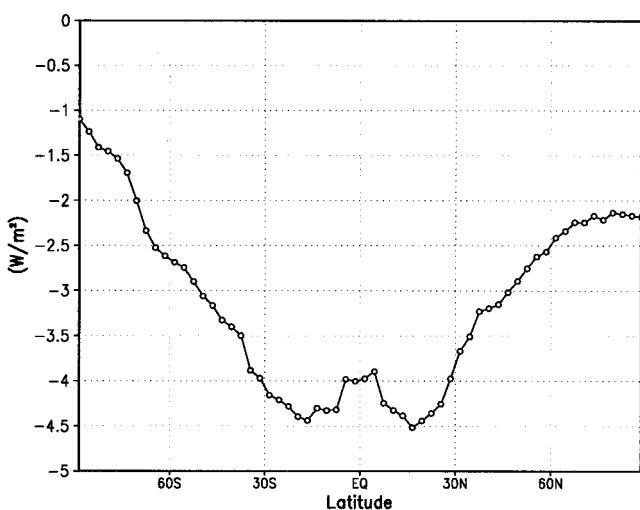


Figure 4. Instantaneous change in zonally averaged net infrared flux (in W/m^2) at the tropopause due to the effects of trace species and halocarbons. Calculations employ atmospheric temperature, species, and cloud profiles taken from a SKYHI GCM 3gas simulation on a model January 1, April 1, July 1 and October 1 dates; results shown are the average of the four calculations. Negative values imply increased infrared flux into the surface-troposphere system. The H_2O continuum effects are evaluated using the RSB algorithm in both cases.

Table 3 is a summary of the absorbers and frequency bands used in each of the frequency domains included in the SEA formulation. The APPROX column gives the bands and absorbers included in the Q^{APPROX} and $Q_{\text{CTS}}^{\text{APPROX}}$ terms, while the CTS column gives the same quantities for the Q_{CTS} term.

3. Model Calculations: Effects of Inclusion of CH_4 , N_2O , and Halocarbons

3.1. GCM Results

The SEA formulation described in section 2 has been incorporated into the GFDL troposphere-stratosphere-mesosphere general circulation model (the “SKYHI” GCM, described by Hamilton *et al.* [1995]). The version of the model used in this paper contains 40 vertical levels, at ~ 1 km resolution in the troposphere, increasing to ~ 2 km in the stratosphere and somewhat larger in the mesosphere. The longitude-latitude resolution used here is 3.6° by 3.0° . The GCM uses prescribed clouds, varying in latitude and season; each grid point is assumed to be partly covered with three randomly overlapped low, middle, and high clouds. Sea surface temperatures are also prescribed, varying seasonally and with longitude and latitude. Ozone concentrations are annually averaged, varying only in latitude and height. CO_2 , CH_4 , and N_2O concentrations are fixed at 356 ppmv and 1714 and 311 ppbv, respectively, at all latitudes, using IPCC-prescribed surface values for 1992. Concentrations for CFC-11, CFC-12, HCFC-113, and HCFC-22 are 268, 503, 82, and 105 parts per trillion by volume (pptv), respectively, at all latitudes. The trace gases and halocarbons are assumed to be uniformly mixed from the surface to the top of the atmosphere. It should be noted that measured CH_4 and N_2O concentrations decrease considerably below ~ 30 hPa [Randel *et al.*, 1998; Jones and Pyle, 1984]; thus in this region the temperature differences between the model calculations described below are likely to be overestimates.

Model integrations have been performed for two cases, with varying numbers of radiatively active species: (1) H_2O , CO_2 , and O_3 (the three-gas (3gas) case), which serves as the control experiment; and (2) H_2O , CO_2 , O_3 , CH_4 , N_2O , plus four halocarbons (the 9gas case). In both of these experiments the H_2O continuum has been treated using the RSB algorithm.

Figure 4 displays the change in the zonally averaged net flux at the tropopause between the 9gas and the 3gas cases using the same GCM-derived initial temperature and moisture profiles. The results shown are the average of four calculations

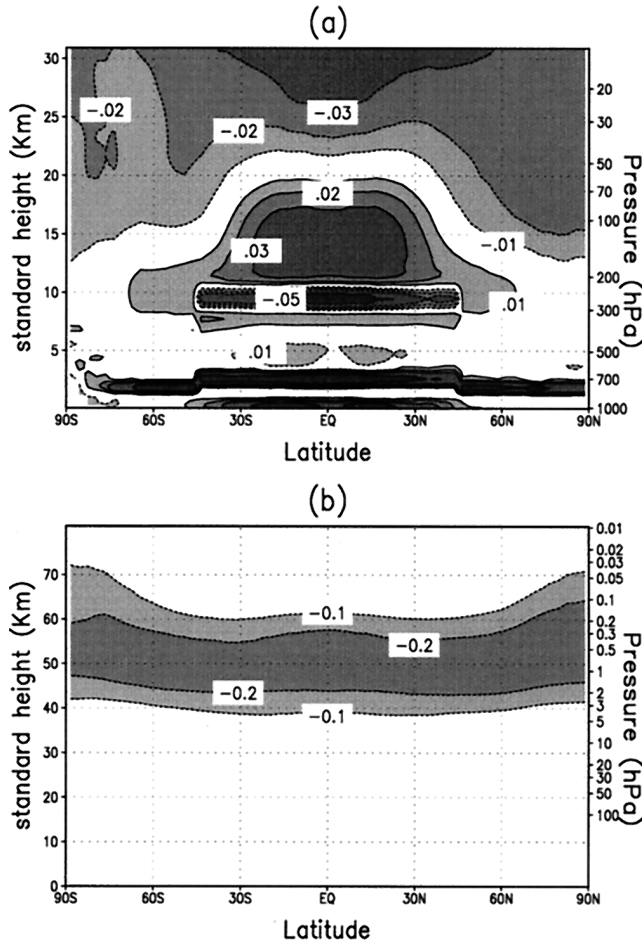


Figure 5. Instantaneous change in zonally averaged infrared heating rates (in K/d) due to the effects of trace species and halocarbons but not the H₂O continuum. Atmospheric profiles are the same as in Figure 4. Figure 5a emphasizes the troposphere and Figure 5b the middle atmosphere.

using model January 1, April 1, July 1, and October 1 profiles. As in the work of *Ramaswamy et al.* [1992], the definition of the tropopause is arbitrary, ranging from 100 hPa at the equator to 300 hPa at each pole, with a linear increase in latitude. The annually averaged change reaches ~ -4.5 W/m² in tropical latitudes, decreasing to ~ -2 W/m² at the North Pole and ~ -1 W/m² at the South Pole. The corresponding zonally averaged instantaneous heating rate change between the 9gas and the 3gas cases is shown in Figure 5a, for altitudes below ~ 30 km, and in Figure 5b for the entire 0–80 km region. In the troposphere the most important effect is a heating of ~ 0.03 K/d in the vicinity of the tropical tropopause. The concentrated regions of cooling at ~ 10 km and heating at ~ 3 km in the tropics are a model artifact stemming from the presence of prescribed clouds at these altitudes. In the middle atmosphere, instantaneous heating rate changes exceed -0.2 K/d near 50 km in all latitudes. These changes are quite similar to the heating rate changes computed by the LBL and SEA methods for the MLS profile (Figures 1e–1f).

The present GCM simulations extend over 10 model years (for the 3gas case) and 11 model years (for the 9gas case) starting from the same atmospheric state (a model January 1). Results for each case are averages of the final 10 model years, either for the annual average or for the Northern Hemisphere

winter (December to February) or summer (June to August) seasons. Figure 6 displays the zonally and annually averaged GCM temperature response to the introduction of CH₄, N₂O, and the four halocarbons. Also shown (with a solid line) are the regions where this response has a statistical significance of greater than 99% (according to a Student *t*-test, assuming statistical independence for each month). Temperature changes near the surface are small, because of the imposition of a prescribed sea surface temperature. The principal result is an increase exceeding ~ 1 K in the tropical upper troposphere (~ 12 – 18 km) and a general decrease of 0.5–1 K in the middle atmosphere; the largest decreases are ~ 1.5 K at the tropical stratopause (~ 50 km). The regions of positive and negative temperature responses occur at similar altitudes to the regions of positive and negative heating rate changes (Figure 5). The annual-mean middle-atmosphere temperature response is statistically significant only in latitudes equatorward of $\sim 35^\circ$. Results for the Northern Hemisphere winter and summer (not shown) indicate that the middle-atmosphere temperature response is also statistically significant through most of the summer hemisphere. The lack of significance of the temperature changes in polar regions in winter is probably due to the limited time extent of the model integration, together with the large model interannual variability in temperature observed in these regions [Hamilton, 1995].

3.2. Radiative Versus Dynamical Response

To study the role of radiation and dynamics in determining the GCM temperature response to a radiative perturbation, the equilibrium GCM zonal-mean, annual-mean temperatures at pressure p (at a given latitude) may be obtained using

$$0 = \frac{\partial}{\partial t} T_{\text{control}}(p) = Q_{\text{rad}}((T_{\text{control}})) + Q_{\text{dyn}}((\text{control})) \quad (7a)$$

for the control experiment and

$$0 = \frac{\partial}{\partial t} T_{\text{pert}}(p) = Q'_{\text{rad}}((T_{\text{pert}})) + Q_{\text{dyn}}((\text{pert})) \quad (7b)$$

for the perturbation experiment. In the above relations, Q_{rad} denotes the heating rate at pressure p obtained using the SEA formulation in the control case; the heating rate principally depends on the equilibrium temperature profile (T_{control}). Q'_{rad} is the corresponding heating rate when the SEA formulation is applied in the perturbation case; the heating rate depends on the perturbation equilibrium temperature profile (T_{pert}). $Q_{\text{dyn}}((\text{control}))$ represents all of the nonradiative contributions to the heating rate, which depends on the values of a number of atmospheric parameters at various latitudes and pressures (denoted here as (control)). $Q_{\text{dyn}}((\text{pert}))$ is the corresponding quantity for the perturbation experiment. We further define the initial heating rate change

$$\delta Q_{\text{init}}(p) = Q'_{\text{rad}}((T_{\text{control}})) - Q_{\text{rad}}((T_{\text{control}})), \quad (8a)$$

the equilibrium radiative heating rate change

$$\delta Q_{\text{rad}}(p) = Q'_{\text{rad}}((T_{\text{pert}})) - Q_{\text{rad}}((T_{\text{control}})), \quad (8b)$$

and the equilibrium dynamical heating rate change

$$\delta Q_{\text{dyn}}(p) = Q_{\text{dyn}}((\text{pert})) - Q_{\text{dyn}}((\text{control})) = -\delta Q_{\text{rad}}(p). \quad (8c)$$

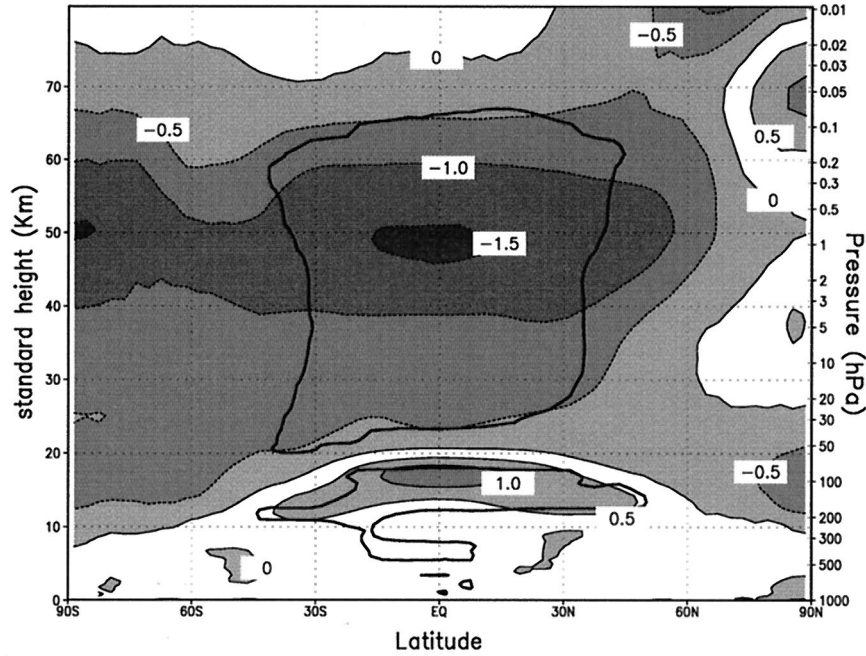


Figure 6. Time-averaged change in zonally averaged temperature (K) between SKYHI 9gas and 3gas GCM simulations. The solid line denotes statistical significance at the 99% confidence level, according to the Student t -test.

If the model atmospheric response at a particular location and altitude is similar to a pure “radiative” response, we obtain

$$\delta Q_{\text{dyn}}(p) = -\delta Q_{\text{rad}}(p) = 0 \quad (9a)$$

and from (7a)

$$Q_{\text{dyn}}(p) = -Q_{\text{rad}}(T_{\text{control}}). \quad (9b)$$

This response is equivalent to that obtained using the fixed dynamical heating (FDH) assumption [Fels and Kaplan, 1975; Ramanathan and Dickinson, 1979; Fels et al., 1980], although the possibility that the GCM may be responding to a number of dynamical changes which mutually offset each other has not been excluded. If the GCM response is radiative, the temperature change between the GCM perturbation and the control simulation depends only on the initial heating rate change. This may be shown by noting that (using (7a), (7b), and (9a))

$$Q_{\text{rad}}(T_{\text{control}}) = Q'_{\text{rad}}(T_{\text{pert}}) \quad (10a)$$

and therefore from (8a)

$$-\delta Q_{\text{init}}(p) = Q'_{\text{rad}}(T_{\text{pert}}) - Q'_{\text{rad}}(T_{\text{control}}). \quad (10b)$$

For sufficiently small temperature changes (10b) may be approximated as

$$-\delta Q_{\text{init}}(p) \approx \sum_{k'} \delta T(P_{k'}) \frac{\partial}{\partial T} Q'(P_{k'}, P_k) \quad (10c)$$

where $\delta T(P_k)$ is the temperature difference between the perturbation and the control equilibrium states at pressure P_k . The most important contribution to the sum occurs when $P_k = P_{k'}$; we thus obtain

$$-\delta Q_{\text{init}}(p) \approx \delta T(p) \frac{\partial}{\partial T} Q'(P). \quad (10d)$$

Since $(\partial/\partial T)Q'(P)$ is negative when the temperature is near equilibrium, one expects a strong positive correlation between $\delta Q_{\text{init}}(p)$ and $\delta T(p)$ when the atmospheric response is radiative.

The reverse situation is one similar to an entirely “dynamical” response, when there is no local thermal response to the local radiative perturbation, or the cooling and heating tendencies from nonlocal radiative perturbations cancel. Under these circumstances one obtains

$$(T_{\text{control}}) \approx (T_{\text{pert}}), \quad (11a)$$

and therefore from Eqs. (8a) and (8b),

$$\delta Q_{\text{init}}(p) \approx \delta Q_{\text{rad}}(p). \quad (11b)$$

One therefore expects a strong positive correlation between $\delta Q_{\text{init}}(p)$ and $\delta Q_{\text{rad}}(p)$ when the atmospheric response is dynamical.

In the present situation, in which the 3gas calculation is the control experiment and the 9gas calculation the perturbation experiment, the atmospheric (zonal mean, annual mean) response appears to be primarily dynamical in the tropical troposphere and mostly radiative in the tropical middle atmosphere. To demonstrate this, zonal-mean, annual-mean values of $\delta Q_{\text{init}}(p)$, $\delta Q_{\text{rad}}(p)$, and $\delta T(p)$ have been computed for all model vertical layers and model latitudes. Figure 7a displays the values of $\delta Q_{\text{init}}(p)$ and $\delta Q_{\text{rad}}(p)$ in the tropical (30°S–30°N) troposphere; the solid line is a least squares fit of the relation between these quantities. Table 4 (rows 1–3) gives the correlation coefficients for the $\delta Q_{\text{init}}(p)$ versus $\delta T(p)$ (radiative), the $\delta Q_{\text{init}}(p)$ versus $\delta Q_{\text{rad}}(p)$ (dynamical) and the $\delta Q_{\text{rad}}(p)$ versus $\delta T(p)$ relationships. The high correlation coefficient (~ 0.92) obtained for the dynamical relationship in the tropical troposphere indicates that the response there to the 9gas perturbation is primarily dynamical in nature.

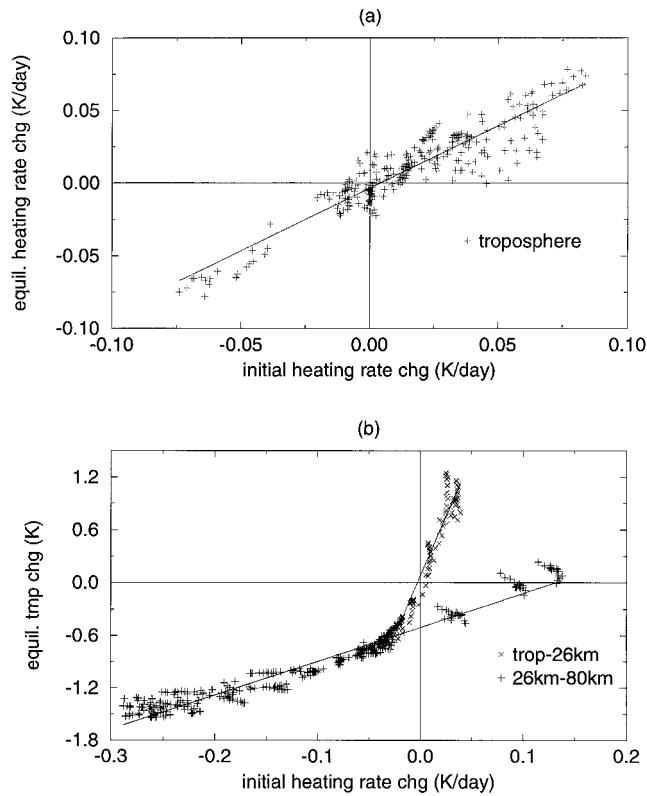


Figure 7. Comparison of the initial infrared heating rate change (zonally averaged) between 9gas and 3gas SKYHI GCM simulations and the zonally averaged change in temperatures and infrared heating rates between the two simulations at equilibrium. (a) Relation between initial heating rate changes ($\delta Q_{\text{init}}(p)$) and equilibrium heating rate changes ($\delta Q_{\text{rad}}(p)$) for vertical layers within the troposphere in the 30°S–30°N latitude range. (b) Relation between the initial heating rate changes and the equilibrium temperature changes ($\delta T(p)$) for two standard altitude regions within the middle atmosphere in the 30°S–30°N latitude range.

In the tropical middle atmosphere the strongest relation between the radiative and the temperature quantities is between $\delta Q_{\text{init}}(p)$ and $\delta T(p)$, with correlation coefficients reaching ~ 0.97 . The atmospheric response in this region is

thus primarily radiative. Figure 7b displays the values of the initial heating rate change and the equilibrium temperature change in the tropics, together with the least squares fit. The model vertical layers have been stratified into two altitude regions: (1) between the tropopause and a standard altitude of ~ 26 km (to capture the lower stratospheric response); (2) between ~ 26 km and the top of the model atmosphere. The slope of the $\delta Q_{\text{init}}(p)$ versus $\delta T(p)$ relation gives a measure of the model radiative-dynamical damping time; we obtain ~ 29 days for the lower stratospheric region and ~ 4.1 days for the region representing remainder of the middle atmosphere. These values, which include nonlocal and dynamical effects, are somewhat smaller than previously obtained radiative-damping time estimates [Fels, 1982; Kiehl and Solomon, 1986].

The extent to which the GCM middle-atmosphere temperature response to the 9gas radiative perturbation is radiative may further be quantified by using an off-line radiative-dynamical model in which the change in the dynamical heating rate in this region is set to zero. Companion calculations have therefore been performed in which the middle atmospheric temperatures at equilibrium are those producing a balance between the radiative heating rate and the dynamical heating, obtained using the FDH assumption (equations (9a)–(9b)). Tropospheric temperatures are held fixed in these calculations, in concordance with the finding that GCM tropospheric temperature change is mostly dynamical in cause. The required dynamical heating rate for the control experiment $-Q_{\text{rad}}(T_{\text{control}})$ is computed for annually and zonally averaged profiles of temperature, water vapor, ozone, surface albedo, and clouds from the 3gas experiment. FDH calculations have been performed for each latitude used in the GCM calculations. The radiative transfer algorithm used in the calculations is identical to that for the GCM.

Figure 8a displays the annually averaged temperature change between the 9gas and the 3gas FDH calculations; the difference between the temperature responses of the GCM and FDH calculations is shown in Figure 8b. Comparison with the GCM results (Figure 6) indicates that in most middle atmosphere regions where the GCM temperature response is statistically significant (see Figure 6), the FDH calculation gives a temperature response similar in magnitude and vertical structure to that of the GCM. Since the temperature response in the FDH calculations is necessarily entirely radiative, the similar-

Table 4. Correlation Coefficients, 30°S–30°N

Experiment	Correlation	Middle Atmosphere		Troposphere, 0–trop		
		trop–26 km	26–80 km			
9gas	δQ_{init} versus δT	0.97	0.97	0.20		
	δQ_{init} versus δQ_{rad}	–0.07	–0.74	0.92		
	δQ_{rad} versus δT	–0.25	–0.78	0.16		
Experiment	Correlation	Middle Atmosphere		Troposphere		
		trop–26 km	26–80 km	0–5 km	5–9 km	9 km–trop
CKD	δQ_{init} versus δT	0.43	0.15	0.05	0.65	0.39
	δQ_{init} versus δQ_{rad}	–0.07	–0.25	0.75	0.97	0.92
	δQ_{dyn} versus δT	0.87	0.95	0.22	–0.67	–0.12

Correlation coefficients between changes in values of Q_{init} , Q_{rad} , Q_{dyn} , and temperature in the 9gas and CKD experiments. Column 2 gives the relationship for which the correlation coefficient is evaluated. The standard altitude regions of the troposphere and middle atmosphere in which the calculation is performed are indicated above columns 3–5 for the 9gas experiment and columns 3–7 for the CKD experiment.

ity of the FDH and GCM temperature change patterns is an additional indication that the GCM middle-atmosphere response to the 9gas radiative perturbation is essentially radiative in nature. The magnitudes and signs of the calculated temperature changes are in general agreement with the expectations of a heating in the lower stratosphere due to absorption of infrared radiation by CH_4 , N_2O , and halocarbons and cooling in the upper stratosphere, due to increased cooling to space by the added species [Ramanathan *et al.*, 1985; Ramaswamy and Bowen, 1994].

The annually averaged temperature responses of the FDH and GCM do vary markedly in much of the tropical lower stratosphere, a region where the GCM temperature response has been shown to be statistically significant. Results shown in Figure 8b indicate that in the 15–20 km region the GCM temperature change (a warming of ~ 1 –1.5 K) exceeds that of the FDH by ~ 0.3 K. In the 20–25 km region the GCM temperature change is a cooling of ~ 0.5 K, while the FDH response is a smaller cooling (by ~ 0.2 K). These differences suggest a small but evident dynamical response in the GCM. Figure 9 displays the difference in the zonally and annually averaged dynamical heating rates in the tropics between the 9gas and the 3gas simulations ($\delta Q_{\text{dyn}}(p)$). If the model temperature tendency is small relative to the radiative and dynamical temperature tendency terms, this quantity may be evaluated as $-\delta Q_{\text{rad}}(p)$. (Direct evaluation of this quantity from model circulation and diffusion terms yields a similar result). In the tropical lower stratosphere, regions where the sign of the difference between GCM and FDH temperature responses is positive (negative) correspond to regions with a positive (negative) change in the GCM dynamical heating rate. A more detailed investigation of the GCM response (results not shown) suggests that the positive values for $\delta Q_{\text{dyn}}(p)$ at ~ 18 km near the equator is due to increased advection of warmer air from higher latitudes; regions of negative values of $\delta Q_{\text{dyn}}(p)$ show a relative increase in upward vertical motion.

A second region where the GCM temperature response is affected by changes in the dynamical heating rate is near the tropical stratopause, where the changes in dynamical heating reach ~ -0.04 K/d at ~ 48 km near the equator and near ~ 55 km at 30°N and 30°S (Figure 9), thus resulting in a marked latitudinal gradient in this field. The GCM temperature response near the stratopause also shows a peak near the equator (Figure 6), in contrast to the response seen in the FDH calculation (Figure 8). Further, the altitude of the maximum GCM temperature response near the equator is ~ 48 km, about 1 km lower than the corresponding altitude in the FDH calculation, suggesting the influence of increased dynamical cooling.

The relatively small magnitude of the initial heating rate change in the lower stratosphere (Figure 5b), the small variation with latitude of the initial heating rate change near the tropopause (Figure 5a), and the radiative nature of the GCM temperature response each suggest that the changes in the GCM winds will be modest. This is confirmed by the results of Figure 10, which displays the change in the annual-mean zonal-mean zonal wind. In almost every region of the middle atmosphere the changes are small and not statistically significant.

4. Model Calculations: Effects of Inclusion of the CKD Continuum

4.1. GCM Results

The SKYHI GCM has also been employed to evaluate the change in climate due to the introduction of the CKD method

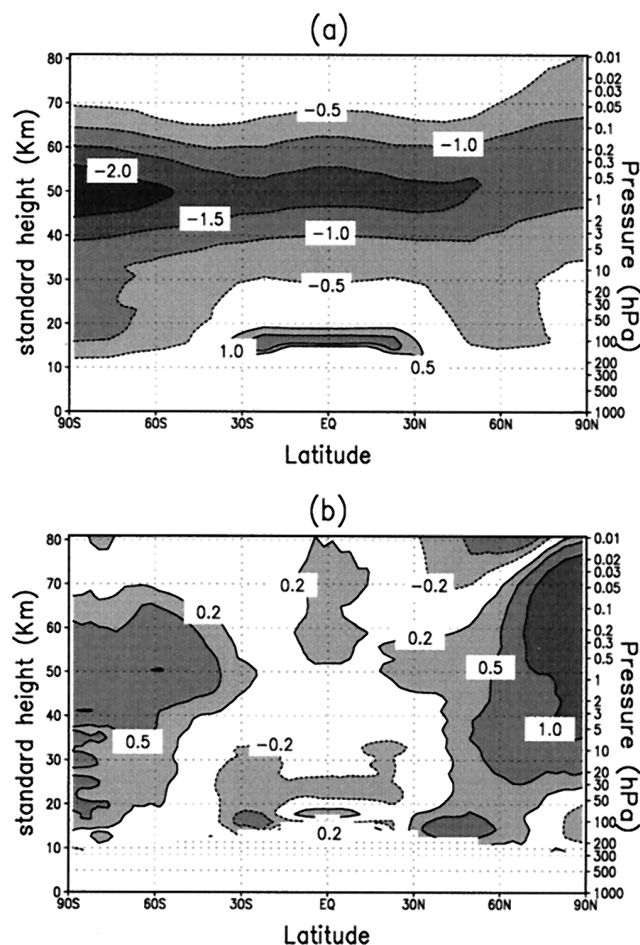


Figure 8. Change in equilibrium temperature between 9gas and 3gas computations using the fixed dynamical heating (FDH) radiative-dynamical equilibrium model (Figure 8a) and difference between time-averaged, zonally averaged temperature changes obtained using GCM simulations for these cases (see Figure 6) and the FDH model results (Figure 8b).

into the SEA radiative formulation. Two simulations have been performed. The first (9gas) has been discussed in section 3; it uses the RSB formulation for the H_2O continuum. The second (CKD) includes all of the trace species included in the 9gas calculation but employs the CKD formulation for the water vapor continuum. In all other respects the model configuration is that described in section 3.

Figure 11 displays the change in the annually and zonally averaged net flux at the tropopause between the CKD and the 9gas calculations using common GCM-generated initial temperature and moisture profiles. As in Figure 4, the results shown are the average of four calculations using model January 1, April 1, July 1, and October 1 profiles. The change reaches ~ -2.5 W/m^2 in most latitudes; smaller values (~ -1.5 W/m^2) are obtained in the antarctic region, where temperatures and moisture amounts are smaller and thus the influence of the H_2O continuum is diminished. These amounts are smaller than the LBL clear-sky values for change in net flux at the tropopause for the MLS profile (Figure 3b), due to the presence of clouds in the GCM, which produces a damping effect on flux changes. The corresponding zonally averaged instantaneous infrared heating rate differences between the CKD and the 9gas cases are shown in Figure 12 for altitudes

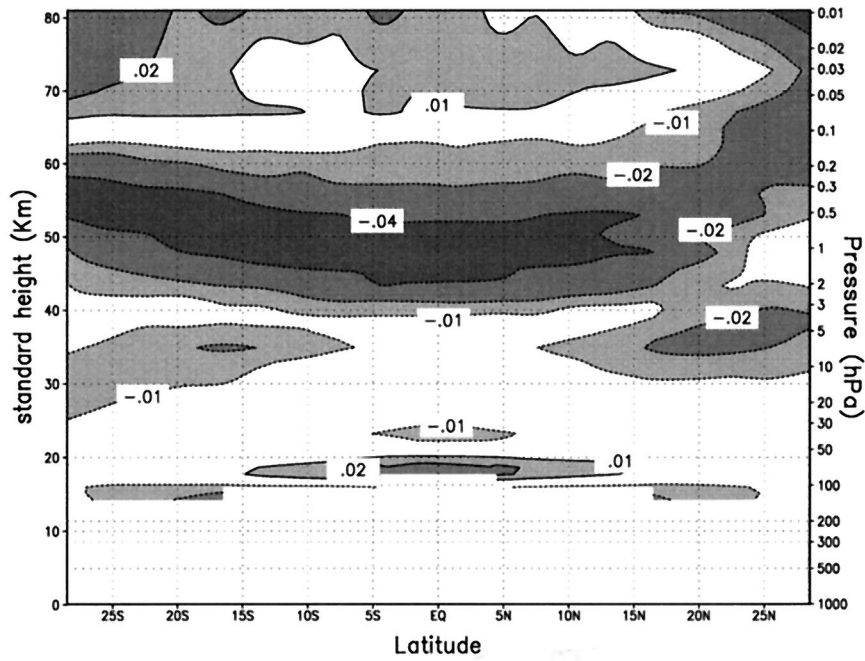


Figure 9. As in Figure 6 but for change in time-averaged, zonally averaged dynamical heating rate (in K/d). The dynamical heating rate change is the negative of the radiative heating rate change.

below ~30 km. The vertical profile of the heating rate changes, at all latitudes, is qualitatively quite similar to that obtained by the LBL calculations for the MLS profile (Figure 3c); magnitudes are smaller due to the presence of clouds. The change in upper tropospheric infrared heating rates reaches ~-0.25 K/d in the tropics and exceeds -0.3 K/d in northern middle latitudes during summer. As in the LBL MLS calculations, heating rates increase in the CKD case relative to the 9gas case in the midtroposphere, with magnitudes attaining ~0.25 K/d.

The CKD GCM simulation has been run for 11 model years, with averages taken for the final 10 model years. Initial conditions for the CKD simulation are a model January 1 (from the 9gas experiment). Figure 13a displays the zonally averaged, annually averaged temperature changes between the CKD and the 9gas simulations for altitudes below ~30 km; Figure 13b displays the patterns of temperature change for the Northern Hemisphere summer. Regions with a statistically significant response (at 99% significance) are indicated with a solid line.

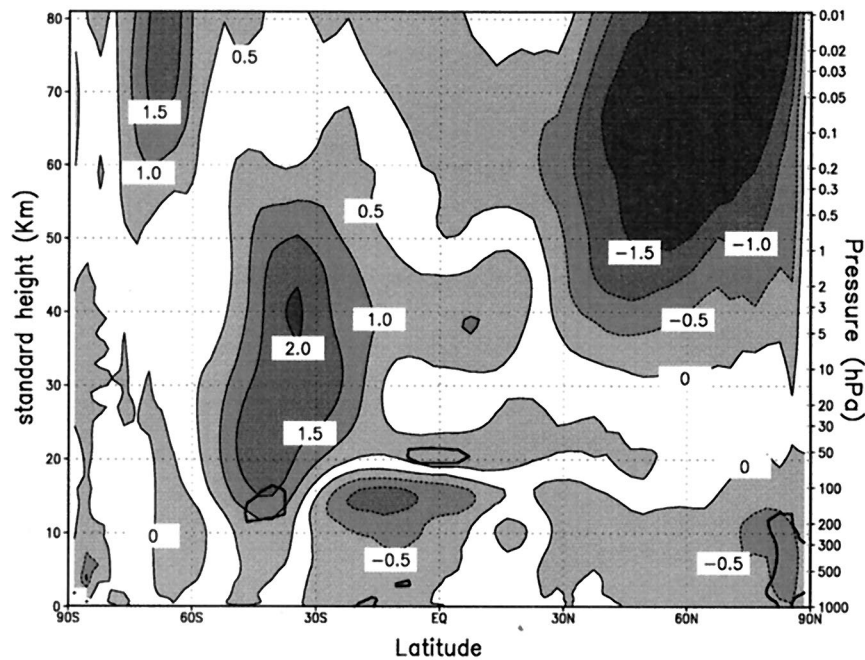


Figure 10. As in Figure 6 but for change in time-averaged, zonally averaged zonal wind (in meters per second (m/s)).

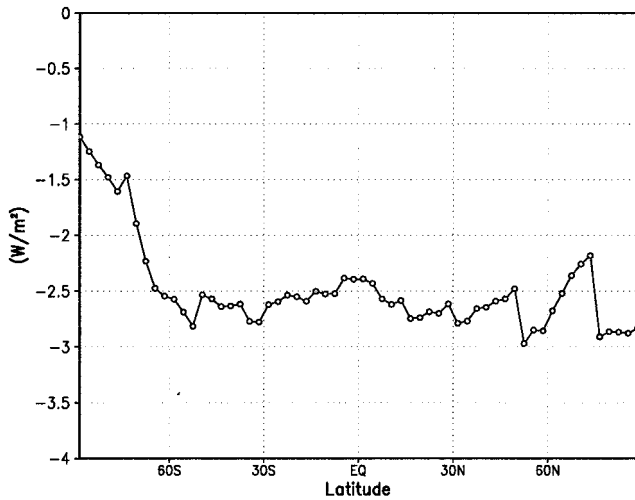


Figure 11. Instantaneous change in zonally averaged net infrared flux (in W/m^2) at the tropopause due to the introduction of the CKD H_2O continuum. Calculations employ atmospheric temperature, species, and cloud profiles taken from a SKYHI GCM 9gas simulation on a model January 1, April 1, July 1, and October 1 dates; results shown are the average of the four calculations. Negative values imply increased infrared flux into the surface-troposphere system.

In both the annual-mean and summer cases, temperature changes above ~ 30 km are mostly under ~ 0.5 K and generally are not statistically significant. The most notable changes are a warming in the lower troposphere (below ~ 4 km), which is statistically significant in the annual-mean tropics and, in summer, throughout the northern hemisphere; cooling of ~ 1 K in the 6–9 km region, significant in most latitudes, especially in summer; and cooling (up to ~ 1.5 K) in the tropical upper troposphere. The altitude of the model tropical tropopause

thus increases slightly (~ 0.1 km). In the tropical lower stratosphere, a significant temperature increase (~ 0.5 – 1 K) is observed in a small region near ~ 25 km. Below ~ 10 km the regions of temperature increases and decreases correspond well to the regions of instantaneous heating rate increases and decreases shown in Figure 12.

The methods described in section 3 (equations (9)–(11)) may be used to determine whether the GCM temperature response can be categorized as primarily radiative or dynamical in nature. Figure 14a displays the relation (and least squares fit) between annually and zonally averaged values of $\delta Q_{\text{init}}(p)$ and $\delta T(p)$ in tropical (30°S – 30°N) latitudes for three layers within the troposphere: (1) between the surface and ~ 5 km; (2) between ~ 5 and ~ 9 km; (3) between ~ 9 km and the tropopause. The choice of these layers is prompted by the pattern of the tropospheric temperature response, i.e., warming in the lower troposphere, pronounced cooling in the midtroposphere, and lesser cooling in the upper troposphere (Figure 13a). According to (10d), a radiative GCM response is diagnosed when the correlation between these quantities is strongly positive. Figure 14b similarly displays the relation between annually and zonally averaged values of $\delta Q_{\text{rad}}(p)$ and $\delta Q_{\text{dyn}}(p)$ for the same tropospheric layers in the tropics. Equation (11b) indicates that a strong positive correlation between these quantities would indicate a dynamical GCM response. Table 4 (rows 4–6) gives the correlation coefficients for the $\delta Q_{\text{init}}(p)$ versus $\delta T(p)$ (radiative), the $\delta Q_{\text{init}}(p)$ versus $\delta Q_{\text{rad}}(p)$ (dynamical), and the $\delta Q_{\text{dyn}}(p)$ versus $\delta T(p)$ relationships in the case of the CKD radiative perturbation. The large positive correlation coefficients for the $\delta Q_{\text{init}}(p)$ versus $\delta Q_{\text{rad}}(p)$ relationship in all three tropospheric regions indicate that the tropospheric temperature response to the introduction of the CKD continuum is primarily dynamical. The only region where a considerable part of the response is radiative is in the 6–9 km region, where the instantaneous change in heating rates between the CKD and the 9gas simu-

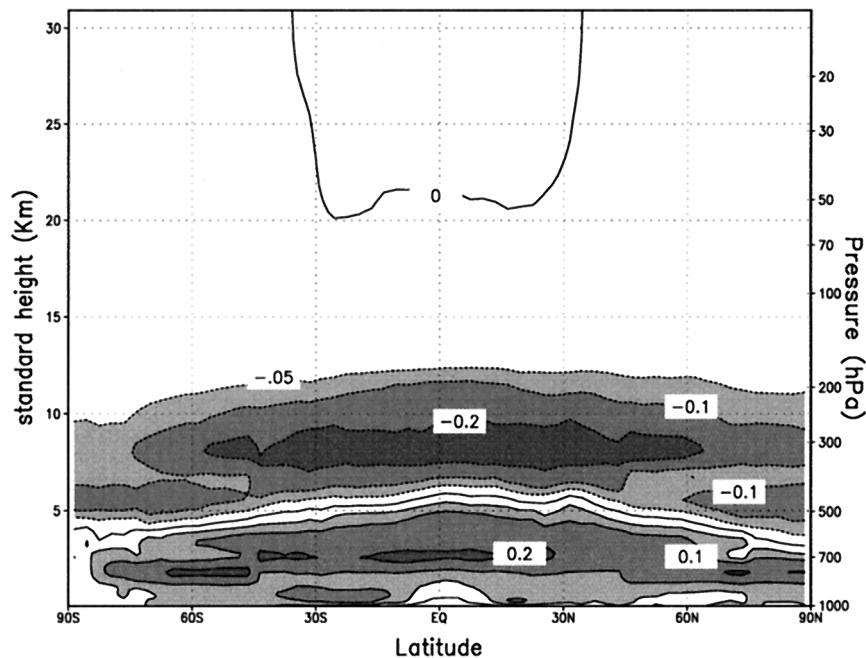


Figure 12. Instantaneous change in zonally averaged infrared heating rates (in K/d) due to the introduction of the CKD H_2O continuum. Calculations and atmospheric profiles are the same as in Figure 11.

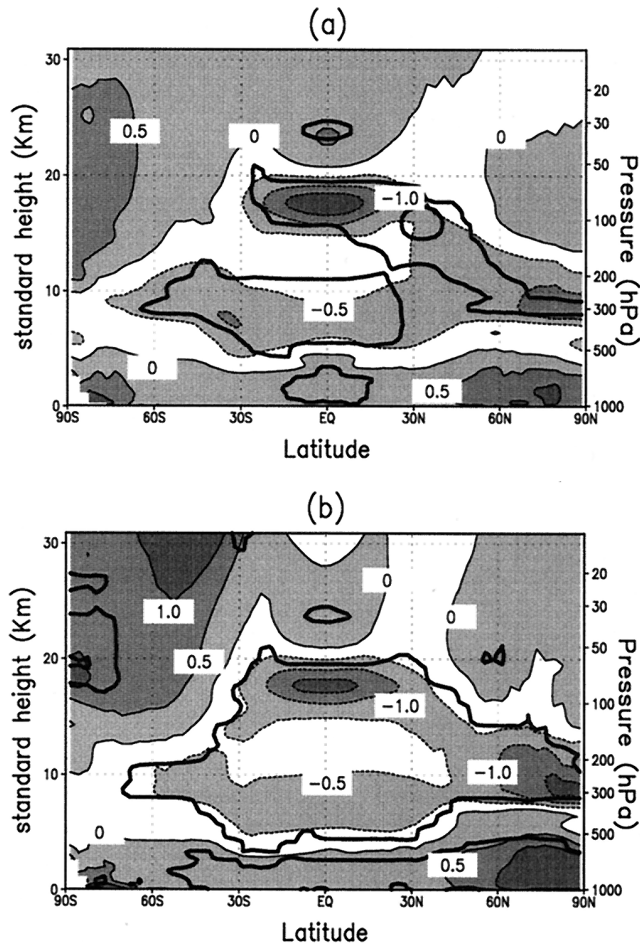


Figure 13. Time-averaged change in zonally averaged temperature (K) between the SKYHI GCM simulation with the CKD H₂O continuum introduced (CKD) and the 9gas simulation. The solid line denotes statistical significance at the 99% confidence level, according to the Student *t*-test. (a) Annually averaged results; (b) results for the Northern Hemisphere summer (June to August).

lations is largest (see Figure 12). Calculations for nontropical tropospheric latitudes (not shown) indicate that the temperature response in those latitudes is also mainly dynamical.

In the middle atmosphere the situation is different; the initial heating rate change ($\delta Q_{\text{init}}(p)$) due to the radiative perturbation is almost zero. Since the introduction of the CKD continuum results in an increase in the downward infrared flux to the troposphere and a reduction of the upward infrared flux (Figure 11), infrared heating rates for equilibrium conditions in the middle atmosphere are generally expected to decrease. If the middle atmosphere the temperature response is radiative, one expects the equilibrium temperature to decrease, with little change in the equilibrium heating rate. By contrast, a dynamical response implies a temperature change controlled by the increase (decrease) in dynamical heating (to compensate for the decrease (increase) in the heating rate). Figure 14c gives the relation (and least squares fit) between $\delta Q_{\text{dyn}}(p)$ and $\delta T(p)$ for the tropical middle atmosphere, divided into two regions as in Figure 7b; correlation coefficients for the relation are shown in Table 4 (row 6). The large positive correlation coefficients indicate that the middle-atmosphere temperature response to the CKD perturbation is indeed mainly dynamical.

A radiative-dynamical relaxation time for the CKD perturbation may be computed using the least squares regression lines; values obtained are ~ 20 days for the lower stratospheric region and ~ 4.1 days for the remainder of the middle atmosphere. The value for the lower stratosphere is smaller than that previously obtained for the 9gas radiative perturbation, probably due to the dynamical nature of the temperature response. The values for the remainder of the middle-atmosphere region are almost the same for the two cases.

The dynamical nature of the response, in the tropical troposphere, to the CKD perturbation implies the presence of changes in the equilibrium zonal-mean circulation. Figures 15a–15b show the zonal-mean vertical velocity change in the

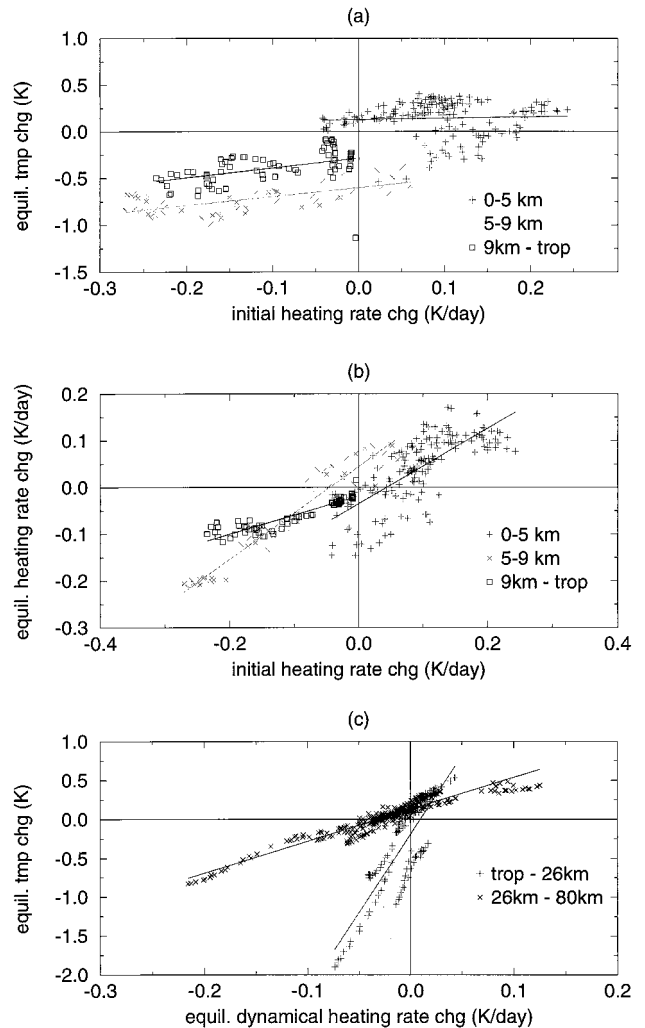


Figure 14. Comparison of the initial infrared heating rate change (zonally averaged) between CKD and 9gas SKYHI GCM simulations and the zonally averaged change in temperatures and infrared heating rates between the two simulations at equilibrium. (a) Relation between initial heating rate changes and equilibrium temperature changes for three standard altitude regions within the troposphere in the 30°S–30°N latitude range. (b) Relation between initial heating rate changes and equilibrium heating rate changes for the same altitude regions. (c) Relation between the equilibrium temperature changes and the equilibrium dynamical heating rate changes ($\delta Q_{\text{dyn}}(p)$) for two standard altitude regions within the middle atmosphere in the 30°S–30°N latitude range.

annual-mean (Figure 15a) and Northern Hemisphere winter (Figure 15b) seasons for the 30°S–30°N latitude range. In both cases, there is an increase in upward vertical velocity near the equator (at altitudes up to ~15 km) and a larger downward motion in subtropical latitudes, suggesting a strengthening of the mean Hadley circulation. A second indication of such strengthening is an increase in the upper tropospheric zonal-mean zonal wind in the tropics and subtropics. Figures 16a–16c display the change in this quantity for the annual-mean (Figure 16a), Northern Hemisphere winter (Figure 16b), and Northern Hemisphere summer (Figure 16c) together with regions of statistical significance (at the 99% level). In the tropical troposphere above ~10 km, the annually averaged zonal-mean zonal wind increases by ~1.5 m/s and by ~2 m/s in winter, with smaller but evident increases in summer. The winter and annually averaged results are statistically significant. An expected consequence of the changes in vertical velocity is a decrease in equatorial upper tropospheric temperatures; this is the likely cause of the temperature decreases computed in the 15–20 km region near the equator (Figures 13a–13b), a region where the change in initial heating rate is small (Figure 12). It is important to note that in all of the GCM simulations discussed in this section and section 3, the cloud amounts, altitude distributions, and properties are fixed. This tends to concentrate heating rate

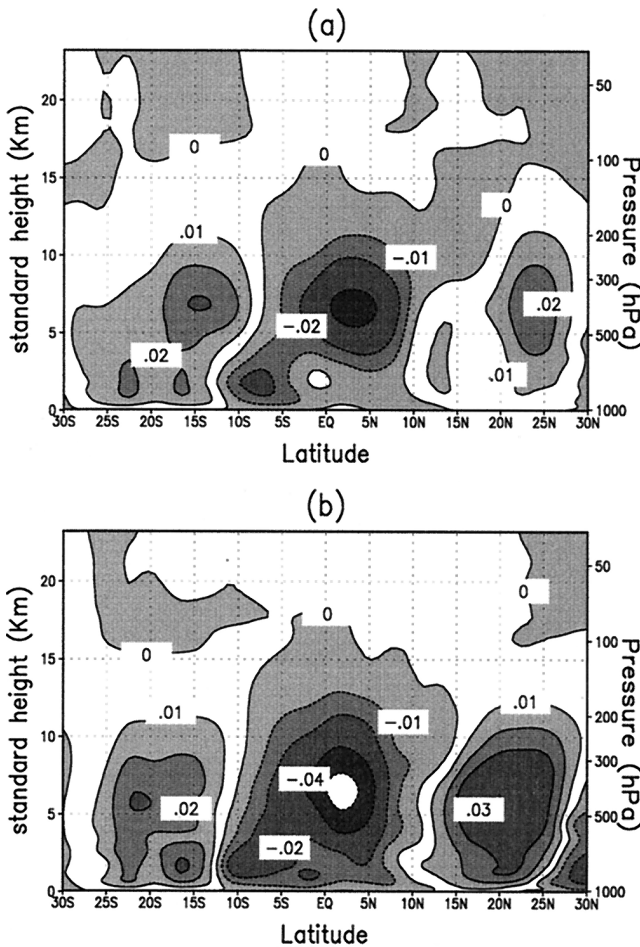


Figure 15. As in Figure 13 but for change in time-averaged, zonally averaged vertical velocity (in 10^{-3} hPa/s). (a) Annually averaged results; (b) results for the Northern Hemisphere winter (December to February).

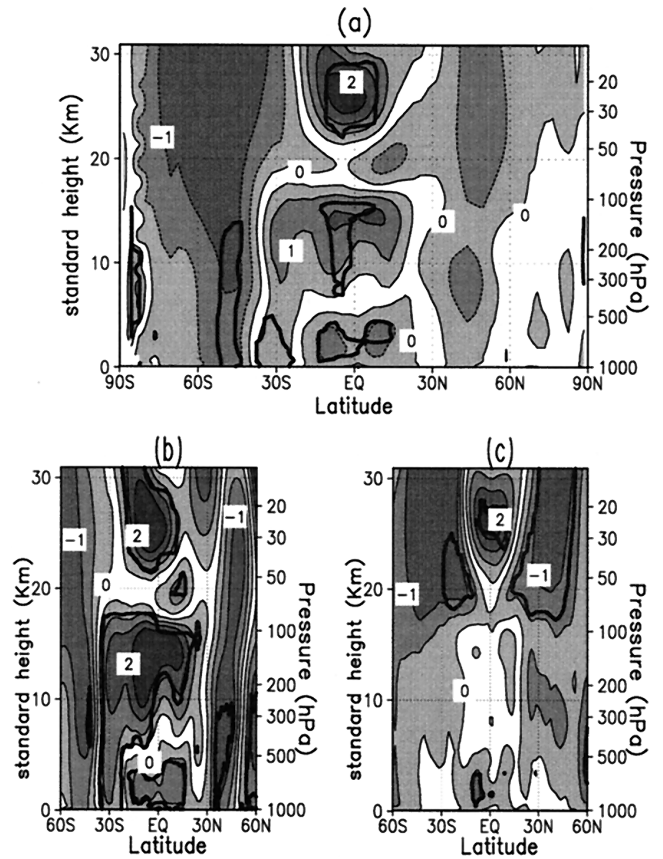


Figure 16. As in Figure 13 but for change in time-averaged, zonally averaged zonal wind (in m/s). (a) Annually averaged results; (b) results for the Northern Hemisphere winter (December to February); (c) results for the Northern Hemisphere summer (June to August).

changes near the locations of the clouds (see Figure 5a) and to preclude any possible feedback effects due to changes in clouds.

4.2. Comparison With Control Experiment

The changes in the annual-mean temperature upon introducing both the trace species and the CKD continuum are shown in Figure 17. Regions of statistical significance (at the 99% level) are shown with a solid line. Temperature changes in the lower and middle troposphere (below ~10 km) are dominated by the effects of the CKD continuum (see Figure 13a); thus the lower troposphere warms and the middle troposphere (~6–9 km) cools. The results are statistically significant in the lower troposphere near the equator and through most of the middle troposphere. Above ~10 km in the troposphere the warming effects due to the trace gases (see Figure 6) become dominant over the cooling effects due to the CKD continuum; tropical temperatures in this region show a statistically significant increase (up to ~0.5 K). Middle-atmosphere temperature changes are dominated by the cooling effects due to the trace gases (Figure 6); in the tropical upper stratosphere the result is a statistically significant 1–1.5 K cooling.

Along with temperature changes, changes in water vapor amount have been computed as a result of the radiative perturbations. Figures 18a–18c display the percentage changes in the zonal-average, annual-mean mixing ratio for the 9gas perturbation (Figure 18a), for the CKD perturbation (Figure 18b)

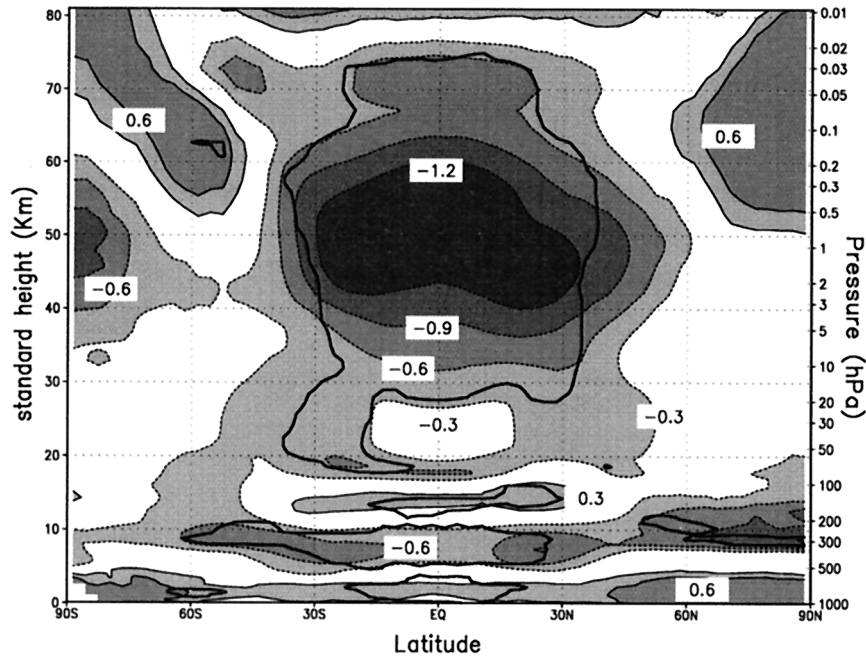


Figure 17. As in Figure 13 but for time-averaged change in zonally averaged temperature between the SKYHI CKD and the 3gas simulations. The results are for the annual average.

and for the combined effect of both perturbations (Figure 18c). Changes in relative humidity for the corresponding perturbations are displayed in Figures 18d–18f. Regions with statistically significant changes in mixing ratio (when effects of both perturbations are included) include the tropical troposphere and most of the lower stratosphere. In the lower and middle tropical troposphere (below ~ 12 km) the changes in water vapor amounts and relative humidity are mainly due to the influence of the CKD perturbation (compare Figure 18b and 18c and Figures 18e and 18f). Mixing ratios in this region decrease by ~ 4 – 8% , while the relative humidity also generally decreases (by ~ 1 – 2%), but increases in the altitude range (~ 7 – 10 km) where temperature decreases (Figure 17) are greatest. Near the surface, where temperatures have actually increased, the decrease in relative humidity is more substantial ($\sim 2\%$). In the 12–17 km region in the tropics, in which temperatures increase, the substantial increase in mixing ratio due to the 9gas perturbation is largely offset by the effect of the CKD perturbation, resulting in a small (statistically insignificant) percentage increase in mixing ratio and a decrease in relative humidity. Above this region the effect of the combined perturbations is a decrease in mixing ratio, associated with temperature decreases in the middle atmosphere. The relative humidity noticeably increases at the tropical tropopause (despite a decreased mixing ratio); such changes are consistent with indications (Figure 15) of an increase in upward vertical velocity in the upper tropical troposphere.

5. Comparison With Satellite Observations

Satellite observations of the outgoing longwave irradiance (OLR) at the top of the atmosphere constitute a measure of the performance of radiative algorithms in GCMs, provided that simultaneous observations of temperature, moisture, trace species, and cloud profiles are available. Because of the uncertainties in determining observed cloud amounts and altitudes,

the comparison is best performed for the clear-sky case. Clear-sky ERBE outgoing longwave irradiances have been obtained for each day of July 1987, as well as daily ECMWF assimilation model temperature, surface pressure and relative humidity profiles for that month. The observed ECMWF profile data (on a $2.5^\circ \times 2.5^\circ$ horizontal grid) and ERBE data have been interpolated to the horizontal resolution of the GCM ($3^\circ \times 3.6^\circ$). The profile data are given at 12 pressures, ranging from 50 to 1000 hPa; within this pressure range, interpolation to SKYHI vertical layers has been performed using the ECMWF surface pressure values. At lower pressures, SKYHI temperature and moisture values (obtained from an average of 10 model Julys in the 9gas simulation) are used. Ozone amounts are taken from the values used by the SKYHI model for July.

Daily irradiance calculations using these data have been performed for the 3gas, 9gas and CKD cases and compared with the ERBE OLR data. Results include only those grid points for which the ERBE clear-sky irradiances for a particular day are available. Figure 19 displays the differences between the calculations of OLR and the clear-sky observations, each zonally and monthly averaged, for the regions between 60°N and 60°S . (Large differences between calculations and observations in polar regions are at least in part due to biases in the ERBE observations and therefore are not displayed). The magnitude and latitudinal distribution of the differences for the CKD case is quite similar to recent calculations [Slingo *et al.*, 1998] which employed a newer version of the ECMWF data.

As might be expected, introduction of the trace species and inclusion of the foreign-broadened water vapor continuum, both of which act as additional absorbers in the upper troposphere) results in a reduction in the outgoing irradiance. The 9gas case gives irradiances ~ 5 W/m^2 less than the 3gas case, while the CKD case results in an additional reduction of ~ 4 W/m^2 . In each case, the differences vary only slightly with

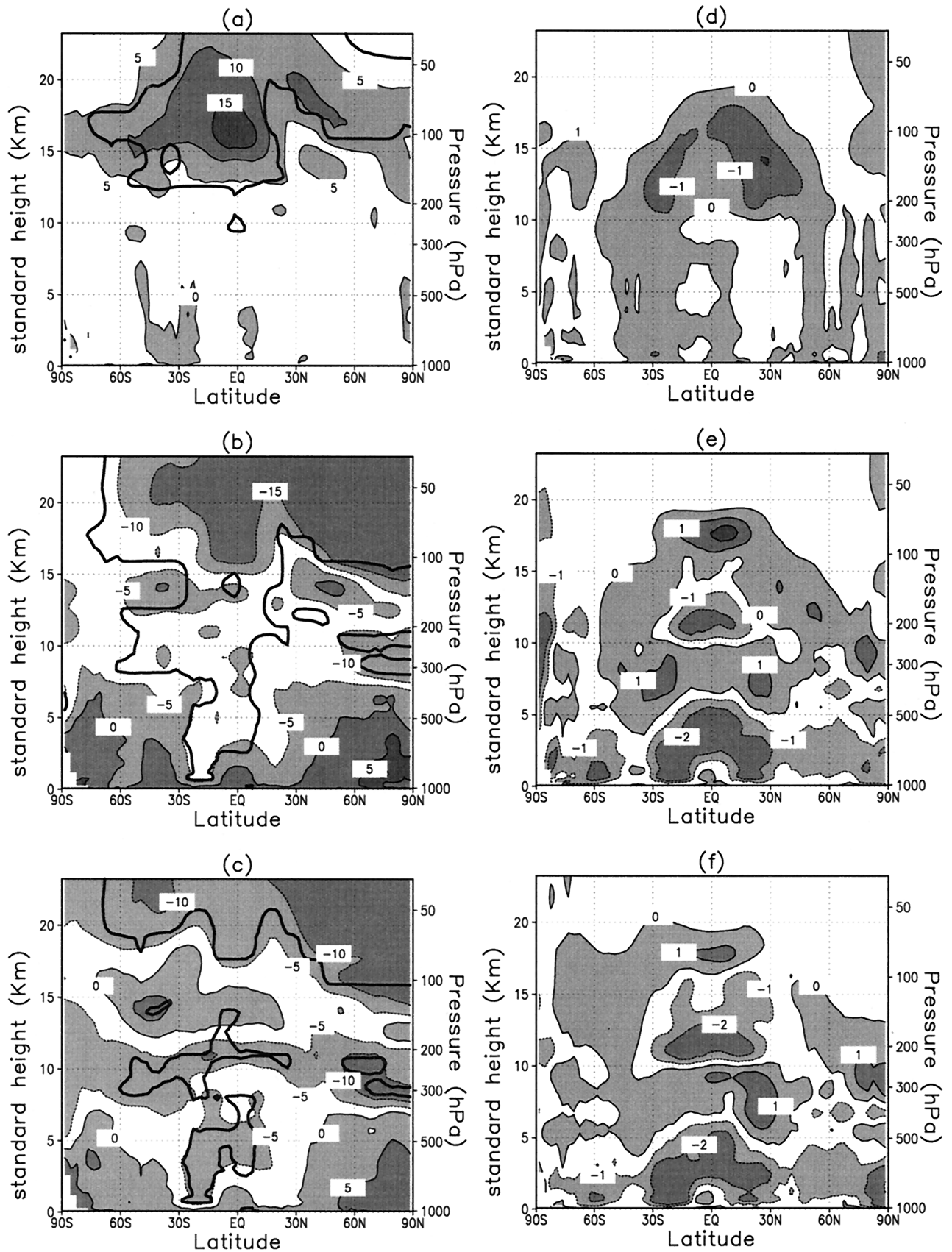


Figure 18. Changes in time-averaged, zonally averaged H_2O mass mixing ratio and relative humidity between GCM simulations. The solid line denotes statistical significance at the 99% confidence level, according to the Student t -test. (a–c) Percentage change in mixing ratio between (a) the 9gas and the 3gas, (b) the CKD and the 9gas, (c) the CKD and the 3gas simulations. (d–f) Change (in percent) in relative humidity between (d) the 9gas and the 3gas, (e) the CKD and the 9gas, (f) the CKD and the 3gas simulations.

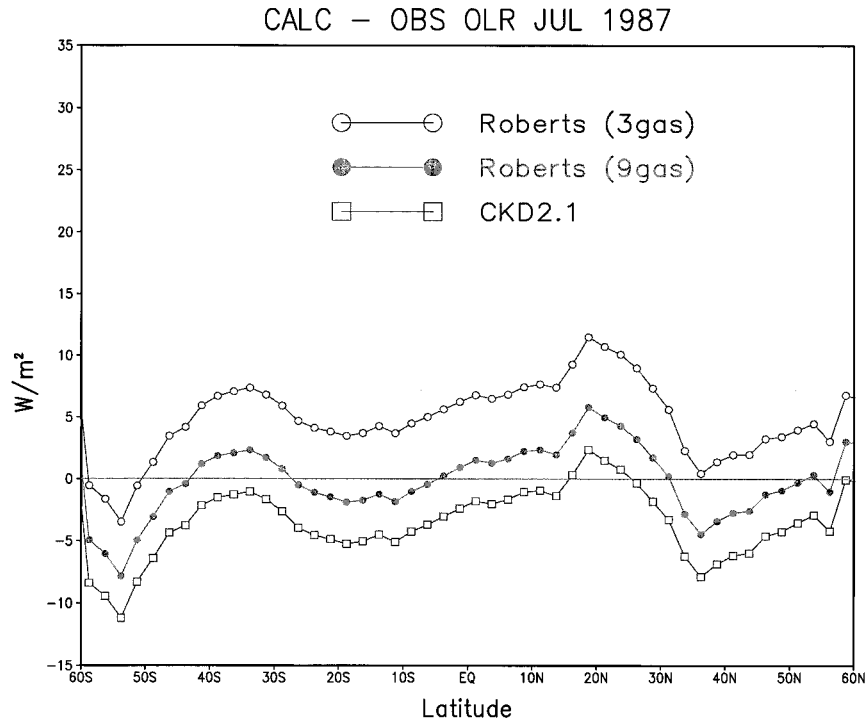


Figure 19. Difference (in W/m^2) between computed and observed clear-sky zonally averaged outgoing infrared irradiances for July 1987. The observational data are from ERBE measurements. The computations use the SEA formulation in the 3gas, 9gas, and CKD cases.

latitude. The changes are somewhat larger than the tropopause flux changes shown in Figures 4 and 11, since those results include the damping effects of clouds. The difference between the CKD and the 9gas cases is quite similar, however, to the value obtained with the clear-sky LBL calculation for the MLS profile (Figure 3b). The insensitivity of the OLR changes to latitude has been corroborated by performing calculations using the RSB and CKD formulations for tropical, subarctic summer, and subarctic winter profiles. A possible explanation is that as the temperature profile varies from tropical to subarctic winter, there may occur in the $160\text{--}560\text{ cm}^{-1}$ frequency range (1) a decrease in the temperature of layers producing the largest contribution to the CTS term in both the RSB formulation (because of the H_2O lines) and the CKD formulation (because of the CKD continuum) and (2) an increase in the temperature difference between these layers (as the H_2O opacity decreases). These two effects tend to produce changes of opposite sign in the OLR.

The 3gas results, which overestimate the outgoing irradiance at almost all latitudes, have the largest differences with observations; however, the $\sim 5\text{ W/m}^2$ bias in the observations [Harrison *et al.*, 1990] suggests caution in stating which case is “best.” Nonetheless, these calculations indicate that the radiative algorithm discussed in the preceding sections is capable of accounting for the observed clear-sky outgoing irradiance to an accuracy of within $\sim 5\text{ W/m}^2$.

6. Summary and Conclusions

This study documents several years of development of the SEA infrared radiative transfer formulation, presently used in GCMs at GFDL and also at other institutions. The SEA method has been adapted to incorporate the effects of trace

gas species (CH_4 , N_2O , and halocarbons) as well as a more complete treatment of the effects of the water vapor continuum, using the CKD formulation. Comparisons of calculations made with the new SEA formulation on standard atmospheric clear-sky profiles with corresponding results obtained using line-by-line methods show that heating rates obtained using the SEA algorithm are within $\sim 0.05\text{ K/d}$ of the LBL values both in the troposphere and in the middle atmosphere. For these profiles, net fluxes computed by the SEA and LBL methods at the surface and the top of the atmosphere agree to within $\sim 0.3\text{ W/m}^2$. These differences do not exceed those documented for the previous version of the SEA method (SF91). Even with the addition of several well-known mechanisms of infrared absorption, the computational burden of the new algorithm is only about 50% more than the previous SEA version; given the rapid increases in computer power and the need to account accurately for fundamentally well-understood radiative processes, this should be an acceptable price.

Two SKYHI GCM experiments with fixed clouds and prescribed, seasonally varying sea surface temperatures have been performed to demonstrate the effects of inclusion of these radiative effects on the climate. In the first experiment the radiation formulation incorporates the effects of trace gas species and halocarbons, while the algorithm for calculating the effects of the water vapor continuum is left unchanged. The initial radiative perturbation produces an instantaneous decrease of $\sim 4\text{ W/m}^2$ in net infrared flux at the tropopause. The equilibrium temperature response consists of an increase in upper tropospheric temperatures, because of absorption by all of the added species. In the middle atmosphere the addition of CH_4 and N_2O results in cooling, especially near the mesopause. Statistically significant changes are observed in the vi-

cinity of the tropical tropopause and throughout the tropical middle atmosphere; the temperature changes are also significant in the summer hemisphere polar regions of the middle atmosphere. In the region above ~ 30 hPa these temperature responses are probably overestimates of the effects of these gases in the present-day atmosphere, due to the use of a constant vertical profile for CH_4 and N_2O concentrations. Comparison of the initial radiative perturbation with the equilibrium middle-atmosphere temperature and heating rate responses indicates that the middle-atmosphere response in the tropics is primarily radiative in nature. In consequence, companion FDH calculations give a temperature response similar to that obtained using the GCM. The radiative-dynamical damping rates obtained using this model are of the order of 29 days in the lower stratosphere; these decrease to ~ 4 days in the upper stratosphere.

In the second GCM experiment the effects of the water vapor continuum are included using the CKD continuum formulation. In this case, the radiative perturbation produces an instantaneous change of ~ 2.5 W/m^2 in the net infrared flux for tropical latitudes. The equilibrium temperature response, however, is substantially different from the first experiment, as lower tropospheric temperatures increase, while upper tropospheric temperatures decrease. The tropospheric temperature response is largely due to dynamical changes; among these are a statistically significant increase in zonal-mean zonal wind in the tropical upper troposphere, especially in the Northern Hemisphere winter, along with a strengthening of the mean Hadley circulation.

Comparison of temperature results from the GCM simulation including the radiative effects of both the trace species and the CKD continuum to the simulation excluding these radiative effects indicates that the CKD effects are dominant below ~ 10 km, thus producing warming in the 0–5 km region and cooling in the 6–9 km region. At higher altitudes the effects of the trace species predominate, resulting in warming of the tropical upper troposphere and cooling in the middle atmosphere. Except near the surface, a small decrease in moisture is found; the sign of the moisture changes generally correspond to the sign of the temperature changes between the simulations. Since tropical upper tropospheric temperatures computed by the SKYHI model have generally exhibited a negative bias of ~ 10 K, the small increase obtained here (~ 1 K) is welcome but insufficient to explain the discrepancy, which is more likely linked to the fixed cloud amounts and altitude distributions used in these simulations.

Outgoing longwave irradiances computed using the new SEA formulation have been compared to satellite-measured irradiances for clear-sky profiles; results indicate that the GCM algorithm computes irradiances to within ~ 5 W/m^2 . The clear-sky outgoing longwave irradiance decreases by ~ 8 W/m^2 upon introduction of the new absorbing species and the CKD continuum. For most latitudes the results with the new formulation appear closer to observations than those made without inclusion of the new species.

Several improvements to the new formulation are planned in the future. These include adding the capability to employ time-dependent values for CO_2 , CH_4 , and N_2O . At present, separate off-line calculations for the desired volume mixing ratio of these species must be performed, prior to any GCM simulation, using the methods given in SF85. A revised trace species interpolation algorithm, greatly improved in both accuracy and speed, has been developed and will be detailed in a future

paper. Inclusion of this algorithm in the GCM radiation formulation will enable the present formulation to be used in simulations when CO_2 , CH_4 , or N_2O vary with time. A second desirable improvement is the inclusion of nongrey infrared absorption due to particulates, including both aerosols and clouds. Aerosol absorption has been shown to be a significant contribution to middle-atmospheric heating rates following volcanic eruptions [IPCC, 1995]. A related improvement would be the capacity to allow for frequency-dependent cloud emissivities. Such quantities may be derived from cloud parameterizations being implemented in present-day GCMs. The formulation described in this paper allows for nonunity emissivities, which may vary with altitude and (for multilayer clouds) with location within the cloud; however, only one value is permitted in all frequency ranges. Changes to the present formulation to permit inclusion of the aerosol and cloud emissivity effects are now under development. Finally, changes to the treatment of ozone are planned. These include a more accurate calculation of the 9.3 μm band, probably using the methods given by Rosenfield *et al.* [1991] and the inclusion of the 14 μm ozone complex, which has been shown [Shine *et al.*, 1995] to contribute significantly to the radiative forcing due to changes in stratospheric ozone.

Acknowledgments. A. J. Broccoli, K. P. Hamilton, and two anonymous reviewers made useful comments.

References

- Burch, D. E., Continuum absorption by H_2O , *AFGL Tech. Rep., AFGL-TR-81-0322*, 32 pp., Air Force Geophys. Lab., Hanscom Air Force Base, Mass., 1981.
- Burch, D. E., and R. L. Alt, Continuum absorption in the 700–1200 cm^{-1} and 2400–2800 cm^{-1} windows, *AFGL Tech. Rep., AFGL-TR-84-0128*, 46 pp., Air Force Geophys. Lab., Hanscom Air Force Base, Mass., 1984.
- Christidis, N., M. D. Hurley, S. Pinnock, K. P. Shine, and T. J. Wallington, Radiative forcing of climate change by CFC-11 and possible CFC replacements, *J. Geophys. Res.*, **102**, 19,597–19,609, 1997.
- Clough, S. A., and M. J. Iacono, Line-by-line calculations of atmospheric fluxes and cooling rates, 2, Application to carbon dioxide, ozone, methane, nitrous oxide, and the halocarbons, *J. Geophys. Res.*, **100**, 16,519–16,535, 1995.
- Clough, S. A., F. X. Kneizys, R. W. Davies, R. Gamache, and R. Tipping, Theoretical line shape for H_2O vapor: Application to the continuum, in *Atmospheric Water Vapor*, edited by A. Deepak, T. D. Wilkerson, and L. H. Ruhnke, pp. 25–41, Academic, San Diego, Calif., 1980.
- Clough, S. A., F. X. Kneizys, and R. W. Davies, Line shape and the water vapor continuum, *Atmos. Res.*, **23**, 229–241, 1989.
- Clough, S. A., M. J. Iacono, and J.-L. Moncet, Line-by-line calculations of atmospheric fluxes and cooling rates: Application to water vapor, *J. Geophys. Res.*, **97**, 15,761–15,785, 1992.
- Ellingson, R. G., J. S. Ellis, and S. B. Fels, The intercomparison of radiation codes used in climate models: Long wave results, *J. Geophys. Res.*, **96**, 8929–8953, 1991.
- Fels, S. B., A parameterization of scale-dependent radiative damping rates in the middle atmosphere, *J. Atmos. Sci.*, **39**, 1141–1152, 1982.
- Fels, S. B., and L. D. Kaplan, A test of the role of longwave radiative transfer in a general circulation model, *J. Atmos. Sci.*, **33**, 779–789, 1975.
- Fels, S. B., and M. D. Schwarzkopf, The simplified exchange approximation: A new method for radiative transfer calculations, *J. Atmos. Sci.*, **32**, 1475–1488, 1975.
- Fels, S. B., and M. D. Schwarzkopf, An efficient, accurate algorithm for calculating CO_2 15 μ band cooling rates, *J. Geophys. Res.*, **86**, 1205–1232, 1981.
- Fels, S. B., J. D. Mahlman, M. D. Schwarzkopf, and R. W. Sinclair, Stratospheric sensitivity to perturbations in ozone and carbon diox-

- ide: Radiative and dynamical response, *J. Atmos. Sci.*, *37*, 2265–2297, 1980.
- Fisher, D. A., C. H. Hales, W.-C. Wang, M. K. W. Ko, and N. D. Sze, Model calculations of the relative effects of CFCs and their replacements on global warming, *Nature*, *344*, 513–516, 1990.
- Goody, R. M., and Y. L. Yung, *Atmospheric Radiation: Theoretical Basis*, 2nd ed., Oxford Univ. Press, New York, 1989.
- Hamilton, K. P., Interannual variability in the northern hemisphere winter middle atmosphere in control and perturbed experiments with the GFDL SKYHI general circulation model, *J. Atmos. Sci.*, *52*, 44–66, 1995.
- Hamilton, K. P., R. J. Wilson, J. D. Mahlman, and L. Umscheid, Climatology of the SKYHI troposphere-stratosphere-mesosphere general circulation model, *J. Atmos. Sci.*, *52*, 5–43, 1995.
- Harrison, E. F., P. Minnis, B. R. Barkstrom, V. Ramanathan, R. D. Cess, and G. G. Gibson, Seasonal variation of cloud radiative forcing derived from the Earth Radiation Budget Experiment, *J. Geophys. Res.*, *95*, 18,687–18,703, 1990.
- Intergovernmental Panel on Climate Change (IPCC), *Climate Change: The IPCC Scientific Assessment*, edited by J. T. Houghton, G. J. Jenkins, and J. J. Ephraums, Cambridge Univ. Press, New York, 1990.
- IPCC, *Climate Change 1994: Radiative Forcing of Climate Change and an Evaluation of the IPCC IS92 Emission Scenarios*, edited by J. T. Houghton, L. G. Meira Filho, J. Bruce, H. Lee, B. A. Callendar, E. F. Haites, N. Harris, and K. Maskell, Cambridge Univ. Press, New York, 1994.
- IPCC, *Climate Change 1995: The Science of Climate Change*, edited by J. T. Houghton, L. G. Meira Filho, B. A. Callender, N. Harris, A. Kattenberg, and K. Maskell, Cambridge Univ. Press, New York, 1996.
- Jones, R. L., and J. A. Pyle, Observations of CH₄ and N₂O by the Nimbus 7 SAMS: A comparison with in situ data and two-dimensional numerical model calculations, *J. Geophys. Res.*, *89*, 5263–5279, 1984.
- Kiehl, J. T., and S. Solomon, On the radiative balance of the stratosphere, *J. Atmos. Sci.*, *43*, 1525–1534, 1986.
- Lacis, A. A., and J. E. Hansen, A parameterization for the absorption of solar radiation in the earth's atmosphere, *J. Atmos. Sci.*, *31*, 118–132, 1974.
- Ramanathan, V., and R. E. Dickinson, The role of stratospheric ozone in the zonal and seasonal radiative energy balance of the earth-troposphere system, *J. Atmos. Sci.*, *36*, 1084–1104, 1979.
- Ramanathan, V., et al., Climate-chemical interactions and effects of changing atmospheric trace gases, *Rev. Geophys.*, *25*, 1441–1482, 1985.
- Ramaswamy, V., and M. M. Bowen, Effect of changes in radiatively active species upon the lower stratospheric temperatures, *J. Geophys. Res.*, *99*, 18,909–18,921, 1994.
- Ramaswamy, V., and S. M. Freidenreich, A study of broadband parameterizations of the solar radiative interactions with water vapor and water drops, *J. Geophys. Res.*, *97*, 11,487–11,512, 1992.
- Ramaswamy, V., M. D. Schwarzkopf, and K. P. Shine, Radiative forcing of climate from halocarbon-induced global stratospheric ozone loss, *Nature*, *355*, 810–812, 1992.
- Randel, W. J., F. Wu, J. M. Russell III, A. Roche, and J. W. Waters, Seasonal cycles and QBO variations in stratospheric CH₄ and H₂O observed in UARS HALOE data, *J. Atmos. Sci.*, *55*, 163–185, 1998.
- Roberts, R. E., J. E. A. Selby, and L. M. Biberman, Infrared continuum absorption by atmospheric water vapor in the 8–10 μm window, *Appl. Opt.*, *15*, 2085–2090, 1976.
- Rodgers, C. D., and C. D. Walshaw, The computation of infrared cooling rate in planetary atmospheres, *Q. J. R. Meteorol. Soc.*, *92*, 67–92, 1966.
- Rosenfield, J. E., A simple parameterization of ozone infrared absorption for atmospheric heating rate calculations, *J. Geophys. Res.*, *96*, 9065–9074, 1991.
- Rothman, L. S., et al., The HITRAN molecular database: Editions of 1991 and 1992, *J. Quant. Spectrosc. Radiat. Transfer*, *48*, 469–507, 1992.
- Schwarzkopf, M. D., and S. B. Fels, Improvements to the algorithm for computing CO₂ transmissivities and cooling rates, *J. Geophys. Res.*, *90*, 10,541–10,550, 1985.
- Schwarzkopf, M. D., and S. B. Fels, The simplified exchange method revisited: An accurate, rapid method for computation of infrared cooling rates and fluxes, *J. Geophys. Res.*, *96*, 9075–9096, 1991.
- Shine, K. P., B. P. Brügge, A. S. Grossman, D. Hauglustaine, H. Mao, V. Ramaswamy, M. D. Schwarzkopf, R. van Dorland, and W.-C. Wang, Radiative forcing due to changes in ozone: A comparison of different codes, in *Atmospheric Ozone As a Climate Gas, NATO ASI Ser.*, vol. 132, edited by W.-C. Wang and I. S. A. Isaksen, Springer-Verlag, New York, 1995.
- Slingo, A., J. A. Pamment, and M. J. Webb, A 15-year simulation of the clear-sky greenhouse effect using the ECMWF reanalyses: Fluxes and comparisons with ERBE, *J. Clim.*, *11*, 690–708, 1998.
- Suck, S. H., J. L. Kassner Jr., and Y. Yamaguchi, Water cluster interpretation of IR absorption spectra in the 8–14 μm wavelength region, *Appl. Opt.*, *18*, 2609–2617, 1979.
- Wang, W.-C., G.-Y. Shi, and J. T. Kiehl, Incorporation of the thermal radiative effect of CH₄, N₂O, CF₂Cl₂, and CFC₃ into the National Center for Atmospheric Research community climate model, *J. Geophys. Res.*, *96*, 9097–9103, 1991.

V. Ramaswamy and M. D. Schwarzkopf, NOAA/GFDL, P. O. Box 308, Princeton, NJ 08542. (ds@gfdl.gov)

(Received August 27, 1998; revised December 16, 1998; accepted December 22, 1998.)